Processes and temperatures of FGR formation in chondrites

Pierre-Marie Zanetta, Corentin Le Guillou, Hugues Leroux, B. Zanda, R. Hewins, Guillaume Bellino

HAL Id: hal-03470482
https://hal.univ-lille.fr/hal-03470482v1

Submitted on 5 Oct 2022

Processes and temperatures of FGR formation in chondrites

P-M. Zanetta [a,b,1,*], C. Le Guillou [a], H. Leroux [a], B. Zanda [b,c,d],
R. Hewins [b,c], G. Bellino [a]

[a] *Univ. Lille, CNRS, INRAE, Centrale Lille, UMR 8207 - UMET - Unité Matériaux et Transformations, F-59000 Lille, France*
[b] *IMPMC, Sorbonne Université, MNHN, UPMC Paris, UMR CNRS 7590, 75005 Paris, France*
[c] *EPS, Rutgers Univ., Piscataway, NJ 08854, USA*
[d] *Observatoire de Paris, IMCCE, 75014 Paris, France*

Abstract

In order to understand the nature of the dust that accreted onto chondrules in the nebula and to unravel the conditions of formation of fine grained rims (FGRs), we studied three of the least altered chondrites from different chondrite groups (LL3.00 Semarkona, CO3.0 DOM 08006, CR2.8 QUE 99177) and compared the results with our previous work on the Paris CM chondrite (Zanetta et al., 2021). For each sample, we selected representative rimmed chondrules showing minimal traces of aqueous alteration. We performed high-resolution SEM X-ray chemical mapping to obtain relevant phase abundances and grain size distributions. Four FIB sections were then extracted from each meteorite, two in the rims and two in their adjacent matrix for quantitative TEM analysis. At the microscale, texture, modal abundances and grain size differ depending on the chondrite but also between FGRs and their adjacent matrix. At the nanoscale (i.e. TEM observations), matrices of the four chondrites consist mostly of domains of amorphous silicate associated with Fe-sulfides, Fe-Ni metal, Mg-rich anhydrous silicates and an abundant porosity. The related FGRs in Semarkona (LL) and DOM 08006 (CO) exhibit more compact textures with a lower porosity while FGRs in QUE99177 (CR) are similar to the matrix in terms of porosity. In the three chondrites, FGRs are made of smooth and chemically homogeneous amorphous (or nanocrystalline) silicate with no porosity that encloses domains of porous amorphous silicate bearing Mg-rich anhydrous silicates, Fe-sulfides, Fe-oxides and sometimes metal and Fe-rich olivines. The average compositions in major elements of the amorphous regions are similar for the FGRs and the matrix within a given chondrite (but differ between chondrites). The texture and the chemical homogeneity of the smooth silicate and the fact that it encloses domains of porous amorphous silicate bearing other mineral phases similar to matrix-like material suggests a formation by condensation. Areas that are enclosed in this smooth silicate exhibit Fe-rich olivine formed through Fe interdiffusion that also suggest a thermal modification of the dust accreted to form FGRs. These characteristics indicate a transformation process for the modification of the FGR material similar to the one proposed in our previous work on Paris. We conclude that matrix and FGRs accreted a similar type of dust but FGR material was affected by thermal modification and compaction contemporary with their accretion. For each chondrite, dust accreted onto chondrules under different conditions (dust density, temperature) which led to diverse degrees of compaction/thermal modification of the sub-domains and explain the textural differences observed in FGRs. They accreted on chondrules in a warm environment related to the chondrule formation episode, whereas matrix accreted later in a cooler environment.

---

* Corresponding author.

E-mail address: pierre.marie.zanetta@gmail.com (P-M. Zanetta).

[1] Present address: Lunar and Planetary Laboratory, University of Arizona, Tucson, AZ, USA.

1. INTRODUCTION

Fine-grained rims (FGRs) are located at the interface between chondrules (and refractory inclusions and metal grains) and the matrix. They are present in carbonaceous (CR, CM, CO, CV), ordinary chondrite (OC) and enstatite chondrites (Brearley and Geiger, 1991; Metzler et al., 1992; Zolensky et al., 1993; Lauretta et al., 2000; Zega and Buseck, 2003; Metzler, 2004; Krot et al., 2014; Scott and Krot, 2014; Zanetta et al., 2021). They consist of an unequilibrated assemblage of submicrometric phases but in comparison to the nearby matrix, large (>5 μm) crystalline anhydrous phases such as Mg-rich olivine, pyroxenes and sulfides are absent (Brearley, 1993; Zolensky et al., 1993; Zega and Buseck, 2003; Metzler, 2004; Chizmadia and Brearley, 2008; Zanetta et al., 2021). Rims are chemically comparable to the matrix but are more compact (Metzler et al., 1992; Zolensky et al., 1993; Lauretta et al., 2000; Zega and Buseck, 2003; Greshake et al., 2005; Hanna and Ketcham, 2018; Vollmer et al., 2020; Zanetta et al., 2021).

The favored scenario to explain the origin of FGRs is that dust first accreted onto chondrules in a nebular environment before they were all assembled with the matrix to form parent bodies. Chondrules and their attached FGRs then evolved in a primary parent-body as a function of hydrothermal and metamorphic conditions (Brearley and Geiger, 1991; Metzler et al., 1992; Zolensky et al., 1993; Hanowski and Brearley, 2000; Hua et al., 2002; Leitner et al., 2016; Haenecour et al., 2018; Vollmer et al., 2020). Another scenario invoking a nebular environment is the Kinetic Dust Aggregation (KDA) model, where FGRs are formed through relatively high-speed (order of meters per second to kilometers per second) collisions (Liffman and Toscano, 2000; Liffman, 2019). Scenarios considering parent body aqueous alteration and metamorphism of FGRs initially made of anhydrous material have also been proposed (Brearley and Geiger, 1991; Zolensky et al., 1993; Hanowski and Brearley, 2001; Hua et al., 2002). Zanetta et al. (2021) recently proposed an alternative nebular scenario based on the study of the Paris (CM) chondrite. They observed, in FGRs but not in the matrix, a characteristic micro-texture made of sulfide-rich and sulfide-poor compacted domains of amorphous silicate (as also observed in the CM2 chondrite Y-791198 (Chizmadia and Brearley, 2008), and two CR2 chondrites MIL 07525, and GRA 95229 (Vollmer et al., 2020)). They interpreted this micro-texture as the result of a thermal process, which occurred in the nebula during FGR accretion onto the chondrule and before incorporation into the matrix (i.e. the parent body accretion).

Igneous rims are also observed in different types of chondrite groups (Krot et al., 2014). It has been proposed that these rims can provide insight into chondrule/rim relationship as their properties recorded conditions during chondrule formation (density of dust, temperature, composition of the gas e.g, Krot and Wasson. (1995)). They have distinct textures in comparison to FGRs with more abundant and larger crystalline grain sizes (<40 μm). They are interpreted as the result of melting and crystallization of a previously accreted dust rim through a flash heating event in a nebular environment (Krot and Wasson, 1995; Rubin and Krot, 1996). The possibility that FGRs and igneous rims have a genetic link is thus worth investigating.

The presence of FGRs and igneous rims in different chondrite groups suggests they formed at various times and locations during Solar System formation. Among the different chondrite groups, chondrule and matrix abundances vary significantly, as well as oxidation state and isotopic signatures (Hewins, 1997; Krot et al., 2014; Scott and Krot, 2014; Russell et al., 2018; Hellmann et al., 2020). These particularities reflect the diversity of reservoirs and physical conditions in the disk at their origin and should also affect the nature of the FGRs. The presolar grain abundance and the noble gas signature also indicate that rims were formed under specific conditions in the disk and experienced diverse pathways of aqueous alteration on their parent body(ies) according to the petrologic group and to the chondrite (Metzler et al., 1992; Leitner et al., 2016; Haenecour et al., 2018).

So far, FGRs have been mainly described in altered chondrites. A few recent studies have investigated weakly altered chondrites (Chizmadia and Brearley, 2008; Vollmer et al., 2020; Zanetta et al., 2021), which are the best candidates to have preserved information about the accretion conditions. The analysis of FGRs is challenging because of their small grain size (<5 μm) and potential secondary overprints. Thus, in order to minimize the overprints of secondary parent body processes, we selected three of the most pristine objects in the collections. These chondrites were chosen from various groups (QUE 99177 (CR), DOM 08006 (CO) and Semarkona (LL)) and complete the recent work of Zanetta et al. 2021 on the Paris (CM) chondrite. These chondrites all exhibit a high abundance of amorphous silicate in the matrix (Abreu and Brearley, 2010; Dobrică et al., 2019; Davidson et al., 2019; Dobrică and Brearley, 2020a), a low structural order of the polyaromatic carbonaceous matter (Burton et al., 2012; Bonal et al., 2016; Alexander et al., 2018; Quirico et al., 2018) and a high abundance of presolar grains (Floss and Stadermann, 2009; Nguyen et al., 2010; Haenecour et al., 2018; Nittler et al., 2018). They also belong to the least heated samples based on the chromium standard deviation scale (Grossman and Brearley, 2005; Schrader and Davidson, 2017; Davidson et al., 2019). However, despite their pristine characteristics, they exhibit some low degree of alteration (Rubin et al., 1997; Howard et al., 2009; Howard et al., 2011; Howard et al., 2014; Hewins et al., 2014; Le Guillou et al., 2015b; Dobrică et al., 2019; Dobrică and Brearley, 2020a). The matrix of the CR chondrite QUE 99177 contains minor phyllosilicate, carbonate, and magnetite and was therefore classified as 2.8 by Harju et al., 2014. The LL chondrite Semarkona also shows evidence of aqueous alteration in the matrix with its significant amount of smectite (Hutchison et al., 1987; Alexander et al., 1989a, 1989b; Krot et al., 1997a; Keller, 1998; Dobrică et al., 2019; Dobrică and Brearley, 2020a). The Antarctic CO chondrite, DOM 08006 is characterized by the highest known matrix-normalized abundance of O-rich presolar grains (Nittler et al., 2018). Nonetheless, Davidson et al. (2019) reported some magnetite grains in

DOM 08006 (CO) replacing metal, which could originate from a limited aqueous alteration, either in a parent body environment or during terrestrial weathering. We investigated the least altered area of the selected samples at high spatial resolution, using a high-resolution methodology named ACADEMY in order to compare FGRs and their adjacent matrix (Zanetta et al., 2019). This method consists of integrating results of scanning electron microscopy (SEM), electron probe micro-analysis (EPMA) and transmission electron microscopy (TEM) to quantify the mineralogy and composition of sub-micrometric assemblages. It was developed to obtain a complete petrological description at the submicron scale and over large areas, in order to obtain representative analyses. It also provides quantitative mineralogical characteristics (modal abundances, density variation, grain size and shape). The ACADEMY method is therefore ideal for analyzing large objects with fine granulometry and complex mineralogy such as FGRs or matrix in chondrites.

The questions that arose from previous studies and are addressed here are the following: Is the thermal process advocated for Paris (CM) by Zanetta et al. 2021 also observed in other groups? If chondrite groups form at different times and/or places in the disk, were FGR processed under similar conditions? How does the difference between matrix and rims vary among groups? Lastly, since many chondrules from ordinary chondrites and CR chondrites are surrounded by igneous rims (Krot and Wasson, 1995; Krot et al., 2004a), we expect to make new observations in Semarkona (LL) and QUE 99177 (CR) that could answer another fundamental question: are the formation of igneous rims and of FGRs related?

2. SAMPLES AND METHOD

2.1. Samples

Three chondrites from different groups were selected: QUE 99177 (CR 2.8), DOM 08006 (CO 3.00) and Semarkona (LL3.00). The CO chondrite DOM 08006 (section #99) and the CR chondrite QUE 99177 (section #90) were provided by the Antarctic Meteorite Working Group from the Antarctic Meteorite Collection at NASA Johnson Space Center. The LL chondrite Semarkona (section NS2) was provided by the Muséum National d'Histoire Naturelle (MNHN, Paris).

We selected the least altered areas of each sample. Our criteria comprise the preservation of the chondrule glass, the abundance of metal grains, the scarcity of the phyllosilicates (visible at the micron scale due to their fibrous texture), but also the abundance and size of the nanosulfides (pristine matrix exhibit more abundant and smaller nanosulfides (Abreu and Brearley, 2010)).

2.2. Scanning electron microscopy (SEM)

We used a FEG-SEM JEOL JSM-7800F LV operating at 10 or 15 kV to obtain secondary and backscattered electron (BSE) images (University of Lille). Mosaic images of the entire sections were acquired using the Oxford software.

The pixel size ranged from 0.7 up to 2 μm. These mosaics were imported into the GIS software QGIS® in order to scale the raster and extract statistical information about the size and shape of the components (Fig. S1). Chondrule and rim were identified and encircled (polygon shapefiles) manually. From the polygon areas we estimated the surface, the shape and the radius of the components. For the chondrule type identification we used the descriptions from previous works (Scott et al., 1994). The rim boundaries were drawn using a series of characteristics. 1) Rims are identifiable in BSE images since they have a circular shape that surround the chondrule and are frequently more compact than the matrix (porosity values vary depending on the chondrite and the chondrule). This lack of microporosity in the rim is visible in BSE contrast. 2) The grain size of the anhydrous silicates and sulfides is less than a few microns (<4–5 μm, e.g., (Zanetta et al., 2021)). 3) Open fractures are often visible between the rim and the matrix. These fractures, which originated from a stress concentration, testify to a differential mechanical behavior between the matrix and the rim. All these characteristics are not always observed at the same time. Igneous rims were identified based on the descriptions given in Krot and Wasson, (1995).

An Aztec detector from Oxford Instruments with a silicon drift detector of 80 mm^2 and an ultra-thin window (SDD XMaxN) was used for energy dispersive X-ray spectroscopy analyses (EDS). Quantitative chemical maps were acquired with an acceleration voltage of 6 kV. The maps typically consist of 1024*832 pixels, i.e., an area of ~200*160 μm^2 and a resolution of ~200 nm/pixel with a 35 μs dwell time. A total of 8 maps with a live time of 12–14 h were acquired (2 to 3 per chondrite).

2.3. Electron probe micro-analysis (EPMA)

Chemical compositions of grains identified as compositional endmembers by EDS maps were obtained using the electron micro-analysis technique on a CAMECA SX 100 at the University of Lille. The counts for each element were collected on TAP, LiF and LPET crystals during ~20 sec/element at an accelerating voltage of 15 keV and an intensity of 10 nA. To avoid beam damage during the analysis of carbonates and phyllosilicates, a defocused, 3 μm wide beam, was used instead of the classic 1 μm large focused beam.

2.4. Focused ion beam preparation (FIB) and Transmission electron microscopy (TEM)

For each chondrite, two rimmed chondrules were selected in the least altered areas. Twelve electron-transparent sections were prepared by the focused ion beam (FIB) technique using the FEI Strata dual beam 235 at the Institut d'électronique, microélectronique et de nanotechnologies (IEMN, University of Lille). The FIB sections are grouped by pairs. One FIB section was extracted from the FGR and the other one from the adjacent matrix. Their sizes are typically 20*8 μm and 100–150 nm thick. To prevent the bending of the sections, a thicker bar about 0.5 μm

thick was left in the center that isolates two 7–8 µm wide thinned areas.

The sections were analyzed using a Thermo Fisher Scientific™ Titan Themis (University of Lille) operating at 300 kV. The images were acquired with a high angle annular dark field (HAADF) detector and the EDS analyses were performed using a four-quadrant, windowless, super-X SDD detector system. Hyperspectral maps, about 7–12 µm^2 in area, with a pixel size of ~4 nm, were acquired with an 800 pA current, a dwell time of 2 µs during 3–4 h. These maps were then binned to reach an exploitable S/N ratio. Final pixel sizes used for phase mapping and quantification are in the range 15–24 nm. Quantification was achieved using the Cliff-Lorimer method (Cliff and Lorimer, 1975) and an in-house absorption correction procedure (Morris, 1980; Horita et al., 1987). The k-factors for O, Fe, Mg, Al, S, Ca, and K were experimentally determined using standards (fayalite, forsterite, basalt, rhyolite, serpentine, wollastonite and pyrite). The water contents of the amorphous silicate and phyllosilicates were also quantified. The high detector efficiency at low energy as well as a dedicated absorption correction procedure allowed us to quantify oxygen with a precision of about ± 1 %. Assuming charge neutrality and using a $Fe^{3+}/\Sigma Fe$ ratio of ~70% (Le Guillou et al., 2015a), we then calculated the oxygen excess for species of interest. We attributed this excess to the presence of H_2O or OH group (Le Guillou et al., 2014; Le Guillou and Brearley, 2014). We thus calculated the water content for each pixel.

2.5. ACADEMY methodology

In order to obtain quantitative mineralogical and chemical information from complex phase assemblages on representative areas (several hundred micrometers), we applied the ACADEMY methodology (Zanetta et al., 2019). This method is based on the combination of low-voltage hyperspectral EDS data that allow us to obtain both a high-resolution phase and a density map and on EPMA which provides the chemical composition of each phase. Based on the phase map, we calculate the grain size distribution and the phase modal abundances. We assumed that grains were sufficiently small and randomly distributed to be directly converted from surface to volume ratios. The bulk compositions were ultimately calculated by the combination of the modal abundance, the nominal density and the composition of individual phases acquired with EPMA. At the TEM scale, a phase map per FIB section was obtained using the same procedure.

3. RESULTS

3.1. Sizes of chondrules and rims: large scale, statistical analysis

We investigated the size of high temperature components (mainly chondrules, but also CAI and metal grains) as well as their associated FGRs using the Qgis® software (Fig. S1). For Semarkona (LL) and QUE 99177 (CR), the large size of the components allowed us to analyze the whole section (91.66 and 50.29 mm^2). For the DOM 08006 (CO) we analyzed an area of 5.87 mm^2. It represents 10% of the section and a high number of components (~350, Table 1). The abundance of chondrules, matrix and rims varies according to the chondrite group (Krot et al., 2014; Scott and Krot, 2014). The CO chondrite DOM 08006 exhibits higher abundances of matrix (18 %) in comparison to the CR chondrite QUE 99177 (13 %) and the LL chondrite Semarkona (10%). The three chondrites exhibit lower abundances of matrix in comparison to the CM chondrite Paris (45–60 %) (Hewins et al., 2014; Zanetta et al., 2021).

We obtained statistics on Type I chondrules that are sufficiently abundant (35% for Semarkona (LL) and > 90% for DOM 08006 (CO) and QUE 99177 (CR)) and distinguished the fragmented and non-fragmented Type I chondrules. Other component statistics, in lower abundances, are given in Table S1. As in the Paris (CM) (Zanetta et al., 2021), if one considers only the non-fragmented chondrules, 80% of Type I chondrules are rimmed (Table 2). In comparison, the fragmented components rarely display a FGR (1 to 3%) and are never entirely surrounded. The range of Type I chondrule size and the thickness of their FGRs differ (Table 2, and Table S1). The CR chondrite QUE 99177 exhibits larger chondrule sizes but also thicker FGRs than the CO chondrite DOM 08006 or the CM chondrite Paris. Semarkona (LL) has larger Type I chondrules than Paris (CM) or DOM 08006 (CO) but the thicknesses of the associated FGR are similar to those in these chondrites (Fig. S2 and S3). Semarkona (LL) and QUE 99177 (CR) exhibit larger chondrules and higher abundances of igneous rims with 21% and 8% rimmed objects respectively (vs 3% for the CO chondrite DOM 08006 and 0% for the CM chondrite Paris).

3.2. Description of the chondrule – FGR pairs selected

In all chondrites, FGRs share similar characteristics (Fig. 1, see section 2.2). They consist of a silicate groundmass that embeds nanosulfides (<0.5 µm) and small Mg-rich silicates (mainly olivines and pyroxenes) grains (<1–5 µm). The contact between the FGRs and the matrix is not always sharp. Matrix and FGRs are often distinguished based on the presence in matrix of large (<5 µm) anhydrous silicate grains, which are almost absent in FGRs. The FGRs also appear more compact (Figs. 1 and 2, Table 3 and section 3.5.1). In the following we used a systematic system for the chondrule designation. Each chondrule in the different meteorite is identified by their group and a number, e.g. LL-ch1, LL-ch2, CR-ch1, etc. (Fig. 1).

CR-ch1 and CR-ch2 are both Type I chondrules with large, minimally oxidized metal grains. The FGR and the adjacent matrix have almost the same BSE contrast. However, the matrix and the rims are distinguished based on the numerous tochilinite-cronstedtite intergrowths (TCI) patches that are present in the matrix but are rarer in the FGR. This criterion is combined with the BSE contrast and the small porosity variation. Abundant nanosulfides and anhydrous silicates grains smaller than 1 µm are

Table 1

Characteristics of the different components of the three chondrites deduced from BSE mosaic using the QGis® software. Data on Paris are given here to facilitate comparison between chondrite groups (Zanetta et al., 2021). Proportions of components are determined from the area they occupy in the BSE mosaic. n.a: not analyzed.

	Area	Component parameters		
	Analyzed Area (mm²)	Components	Number	Surface %
QUE 99177 (CR)	50.29	Chon.; metal	68	74.8
		Rims	25	11.9
		Matrix	n.a	13.2
DOM 08006 (CO)	5.87	Chon.; metal	359	66.5
		Rims	55	15.3
		Matrix	n.a	18.2
Semarkona (LL)	91.66	Chon.; metal	316	85.4
		Rims	93	4.6
		Matrix	n.a	9.9
Paris (CM)	30.84	Chon.; metal	1192	34.3
		Rims	77	6.4
		Matrix	n.a	50.3

Table 2

Chondrule type I characteristics deduced from BSE mosaic using the QGis® software. In order to be compared to the FGRs, the igneous rim percentages are also estimated (for non-fragmented type I chondrules only). Percentages do not add up to 100% since chondrules sometimes display both types of rims, and not all chondrules are surrounded by a rim. Data on Paris are given for comparison (Zanetta et al., 2021).

	Non-fragmented Chondrule type I					
	% FGRs	% Igneous rims	Chondrule mean radius	FGR's thickness	Chondrule radius range (µm)	FGR thickness range (µm)
QUE 99177 (CR)	76.7	8.3	489.5	63.5	184.1–1456.4	19.8–160.6
DOM 08006 (CO)	82.8	2.8	90.9	18.8	17.1–343.6	2.6–122.3
Semarkona (LL)	74.4	21.3	271.4	21.5	78.9–1639.5	9.3–61.7
Paris (CM)	82.0	n.d	107.7	22.4	17.8–605.1	5.0–81.1

Table 3

Main petrographic characteristics observed at the SEM scale and comparison between FGRs and adjacent matrix. Data from Paris (Zanetta et al., 2021) are given to facilitate comparison between chondrite groups.

		Anhydrous silicates distribution	Nanosulfides distribution	Characteristic secondary phases			
				Phyllosilicates	TCI	Carbonates	Apatite
QUE 99177 (CR)	FGRs	0–4 µm	0–3 µm	absent	rare	rare	common
	Matrix	1–15 µm	0–5 µm + larger grains (>10 µm)	rare	common	rare	rare
DOM 08006 (CO)	FGRs	1–3 µm	0–3 µm	absent	absent	absent	absent
	Matrix	Mainly > 10 µm	Mainly > 10 µm	absent	absent	absent	absent
Semarkona (LL)	FGRs	0–3 µm	0–3 µm	common	absent	absent	rare
	Matrix	1–10 µm	0–7 µm	common	absent	absent	rare
Paris (CM)	FGRs	0–4 µm	0–4 µm	absent	rare	absent	absent
	Matrix	1–10 µm	0–5 µm + larger grains (>10 µm)	common	common	common	rare

observed in both matrix and FGR. CR-ch2 FGR is enriched in micrometric apatite grains in comparison to the other matrices and FGR (Fig. 2 and Table 3).

CO-ch1 is a Type I chondrule containing large metal grains slightly oxidized on their edges. The matrix and the rim are distinguished based on the lower porosity and brighter BSE contrast of the rim (which is the brightest contrast found in the four chondrites). The adjacent matrix also contains abundant coarse-grained phases (>10 µm), such as numerous Fe-oxides as well as olivine and pyroxene
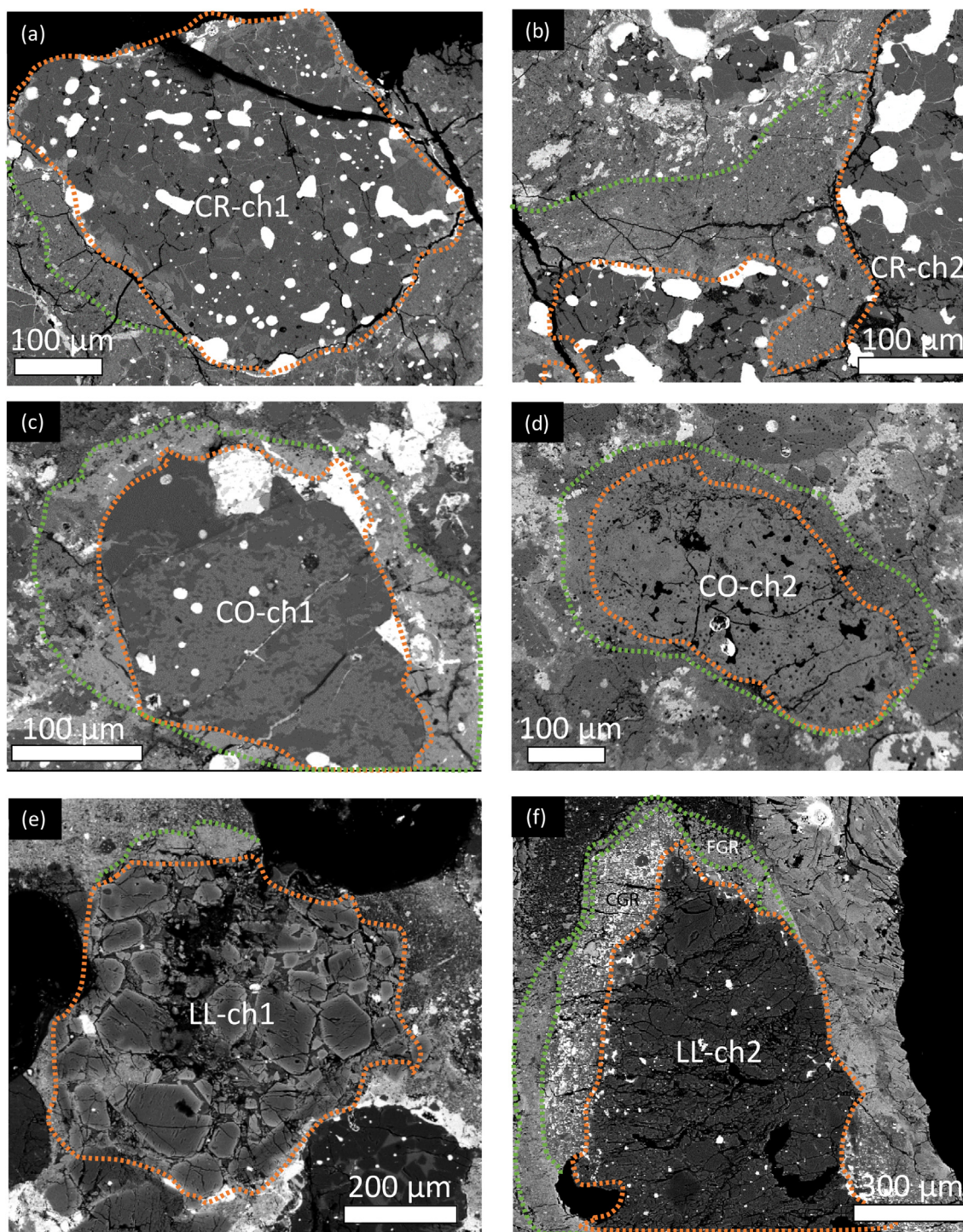
Fig. 1. BSE images of the rimmed chondrules studied. Each sample is identified by two letters. CR is for QUE 99177, CO for DOM 08006 and LL for Semarkona. For each chondrite, two chondrules were selected, numbered 1 and 2. For instance, CR-ch1 stands for chondrule 1 of QUE 99177. The orange line marks the chondrule/FGR border and the green line marks the matrix/FGR border. Different types of chondrules are investigated. They have been selected because they occur within the most pristine areas of the chondrites. a) Type I chondrule in the QUE 99177 CR chondrite. The FGR is only present in the left side of the image near another rimmed chondrule (see Fig. 2). b) Type I chondrule in QUE 99177. The rim fills the embayements in the chondrule. c) Type I chondrule in DOM 08006 with a large metal grain locally oxidized. The FGR surrounds the chondrule completely. d) Type II chondrule in DOM 08006 with a FGR that surrounds the chondrule completely. The porosity is similar to what is found in the matrix. e) Type II chondrule (Semarkona (LL)) in contact with other chondrules. The FGR is only visible on the top part of the chondrule. f) Type I chondrule in Semarkona (LL) with a FGR that surrounds a coarse-grained rim (CGR). The grain size and the abundance of the anhydrous silicates and the sulfides in the coarse-grained rim increase toward the chondrule.
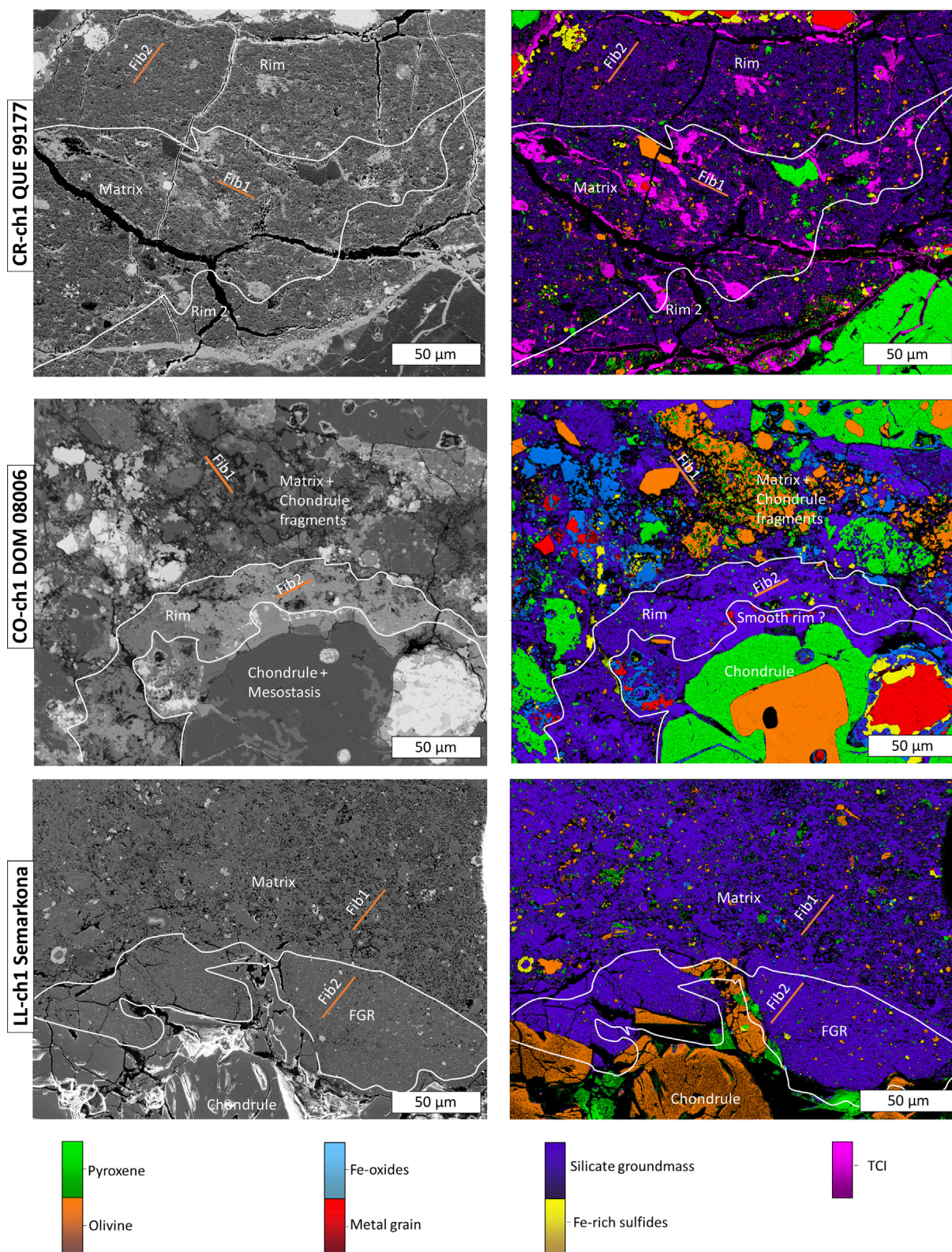
Fig. 2. SEM images and corresponding phase maps obtained from EDS analysis (CR-ch2, CO-ch1 and LL-ch1 chondrules). Contact between components (chondrules, FGR and matrix) are indicated by a white line. The rim 2 indicated in the CR-ch2 images refers to the rim of another rimmed chondrule that is next to the CR-ch2 chondrule. The color scale variation represents the percentage of each given phase at each pixel. This visualization allows us to represent the degree of phase mixing which is significant for the finest material. Fe-rich sulfides regroup troilite, pyrrhotite and pentlandite. Olivine and pyroxene are mostly Mg-rich but rare grains of pyroxene contain Fe and Ca. The legend is limited to the major components for simplification. The silicate groundmass is the most abundant component (purple) in the three chondrites. The presence of coarse grains (anhydrous silicates and sulfides) is an obvious characteristic of the matrix. The localization of the six FIB samples (two for each of the 3 samples) are indicated.

embedded in a -less abundant submicrometric silicate. The matrix is coarser than in the CR chondrite QUE 99177 (Table 3). Most sulfides are coarse-grained, while nanosulfides are almost absent. The CO-ch2 chondrule is a Type II chondrule with a FGR that does not appear compact in comparison to the adjacent matrix. This chondrule was selected for the high porosity of its FGR. The matrix characteristics are similar to the CO-ch1 area.

LL-ch1 is a Type II chondrule. The matrix and the rim are easily distinguished as the FGR appears more compact than the matrix and the differential BSE contrast is clear. The FGR material and the adjacent matrix is fine-grained, mostly submicrometric. Numerous anhydrous silicate grains and sulfides are dispersed in both the matrix and the FGR. These grains are smaller (mostly < 5–10 μm) than those observed in DOM 08006 (CO). LL-ch2 is a Type I chondrule. Its FGR is similar to the one around LL-ch1 chondrule. However, a coarse-grained rim that contains larger anhydrous silicates and sulfide grains (>4μm) than in the outer FGR is observed close to the contact with the chondrule. Both rims are heterogeneously distributed around the chondrule. The surrounding matrix of LL-ch2 is highly porous.

3.3. SEM phase mapping and quantitative mineralogy

Eight phase maps were acquired at the chondrule/matrix interfaces (Fig. 2, Fig. S4 and Table S2). In order to compare the mineralogy of the FGRs and the matrices, the average abundance of the three main types of components was calculated based on the area ratios (fine-grained silicate groundmass, anhydrous silicates (i.e. mostly Mg-rich olivine + pyroxene) and sulfides; Fig. 3). The silicate groundmass refers to the entanglement of phyllosilicate or amorphous silicate with nanosulfides, Fe-oxides and metal grain that cannot be distinguished at the microscale using low-voltage SEM mapping (resolution 250 nm/pixel). Anhydrous silicates and sulfides are always less abundant in FGRs than in the matrix ($3.8 \pm 0.05\%$ vs. $9.7 \pm 0.1\%$ and $0.4 \pm 0.004\%$ vs. $1.8 \pm 0.01\%$ respectively). Hence, the silicate groundmass is always more abundant in FGRs (mean $\sim93 \pm 7\%$) than in the meteorite matrix (mean $\sim80 \pm 6\%$). The abundances of these three components types are comparable in the FGRs of the three chondrites (and in the CM Paris chondrite as well, (Zanetta et al., 2021)). Matrices are more complex: the matrix in DOM 08006 (CO) contains more abundant large anhydrous silicate and sulfide grains and a lower abundance of silicate groundmass (62%) than the matrix of other chondrites. TCI patches in QUE 99177 (CR) chondrite represent $14.2 \pm 1.1\%$ of the matrix (only $6.1 \pm 0.4\%$, in the FGR). In Semarkona (LL), the matrix and the FGR are mineralogically similar to each other, i.e. the same mineral phases are encountered, and the grain size range is mostly inferior to 5 μm.

The grain size distributions of sulfides and anhydrous silicates (Fig. S5) are similar in all the FGRs. The fine-grained population (<4 μm) has a similar size-distribution in the matrix and the FGRs. The matrices in all chondrites always contain an additional population of larger grains (>4 μm). In DOM 08006 (CO), we were able to clearly iden-

tify a dichotomy (Fig. S6). Anhydrous silicate distribution form distinct entities rather than a continuum. In matrices of QUE 99177 (CR) and Semarkona (LL), larger grains (>4μm) are also found, but we could not identify a clear bimodal distribution due to the low number of grains.

3.4. Composition of the analyzed areas

Matrix and rims are depleted in most major elements (except Fe, Ni and Al for the matrix of DOM 08006) in comparison to CI (i.e. once normalized to Si. Fig. 4 a and Table S3, S4 and S5). All chondrites are significantly depleted in S both in the rims and in the matrices (>50% in comparison to the CI composition Fig. 4 a). Most major elements display the same pattern in the FGR and matrix within the same chondrites but differ from one chondrite to another (Fig. 4 a). The CO chondrite DOM 08006 exhibits significant differences in Fe, Ni, Al and S between the matrix and the FGRs. These differences are due to the clastic nature of the matrix which contains large grains that are absent from the FGRs (Mg-rich anhydrous silicates, metal grains and sulfides, clearly visible in the phase map - Fig. 2). In contrast, the compositions of FGRs and matrices of QUE 99177 (CR) and Semarkona (LL) resemble each other. The CR chondrite QUE 99177 is the most depleted in volatile elements (S, K, Na). The LL chondrite Semarkona shows enrichment in K and Na (carried by the silicate groundmass; see section 3.6). The silicate groundmass is close in composition in matrices and FGRs within each of the different chondrites (Table S3).

FGRs show distinct compositions (Fig. 4 b, Table S4 and S5). Semarkona (LL) and Paris (CM) FGRs have higher Al and Ca contents than QUE 99177 (CR) and DOM 08006 (CO) chondrites. Other elements (Ni, Mg and Fe) do not vary systematically. The Mg and Fe are depleted compared to CI but relatively comparable within Semarkona (LL), QUE 99177 (CR) and DOM 08006 (CO). Volatile elements K and Na show the largest Si-normalized variation among the four chondrites.

3.5. Petrography at the TEM scale

3.5.1. Simple layer FGRs

At the TEM scale both matrix and FGRs consist of a fine-grained material dominated by an amorphous silicate which encloses Mg-rich olivines and pyroxenes, Fe-sulfides, rare metal grains and organic compounds (Fig. 5). The major difference between matrices and FGRs is that the FGRs are less porous and show a specific microtexture, previously described in the CM Paris chondrite (Zanetta et al., 2021): about 50% of the FGR sections consist of smooth and chemically homogeneous regions. These regions are several hundreds of nanometers wide and are made of amorphous or nanocrystalline silicate with no porosity. This material encloses domains of porous, amorphous silicate which itself encloses Mg-rich anhydrous silicates (olivine and pyroxene), nanosulfide (mostly troilite), Fe-oxides (mostly magnetite) and sometimes metal (Fig. 5 b,d,f and Fig. 6). The pentlandite is always a minor phase in comparison to troilite in these chondrites. We call these
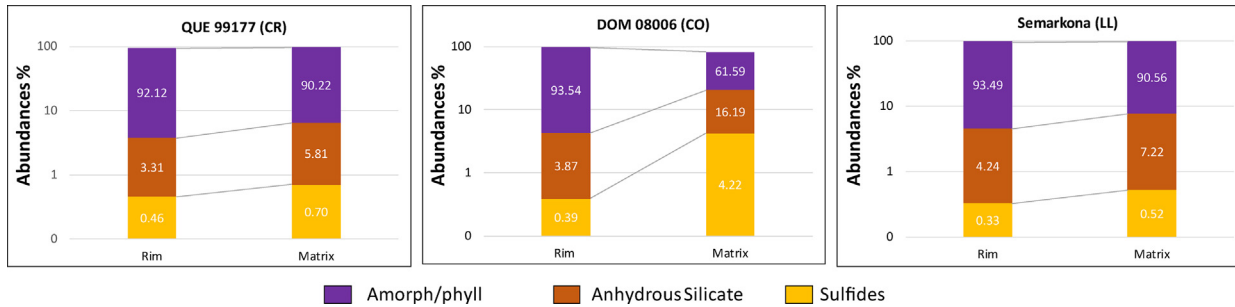
Fig. 3. Modal abundances (logarithm scale) of the main components (amorph/phyll, sulfides and anhydrous silicates) for the FGRs and their adjacent matrix. Amorph/phyll represents the silicate groundmass, a mixture of amorphous silicate and phyllosilicates that cannot be distinguished at the SEM scale. Given that only the main phases are shown, the total is sometimes below 100 %. TCI patches in QUE 99177 (CR) have been integrated to the amorphous/phyllosilicates material.
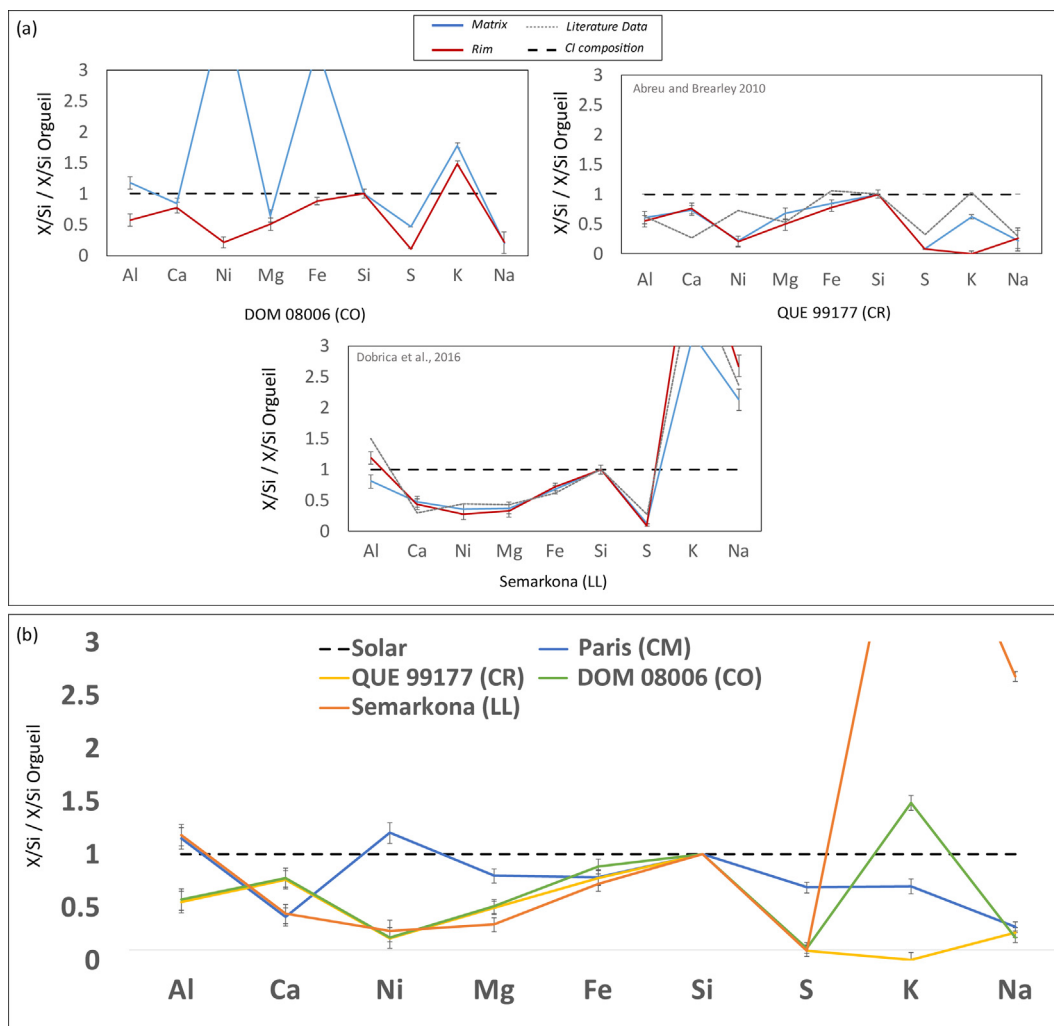

Fig. 4. a) Averaged compositions of matrix and FGRs (this study) for the three chondrites as a function of the 50% equilibrium condensation temperature from (Lodders, 2010). The data are obtained using the ACADEMY method. Values are averaged for each chondrite and normalized to Si and to the CI composition (Lodders, 2010). Matrix compositions from previous studies are plotted (dashed lines) for comparison (QUE99177 (CR) : Abreu and Brearley, 2010; Semarkona (LL): Dobrică and Brearley, 2016) b) Composition of the FGR in the different chondrites. The composition of the inner and outer rims of Paris are averaged (Zanetta et al., 2021).
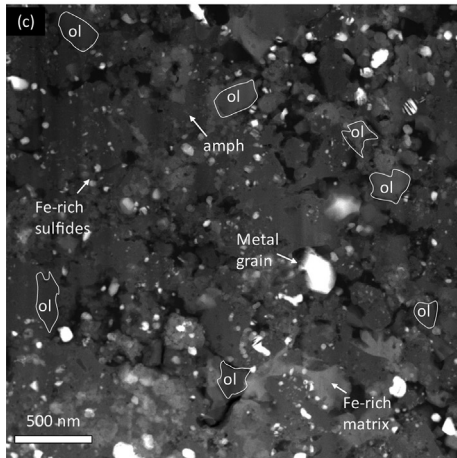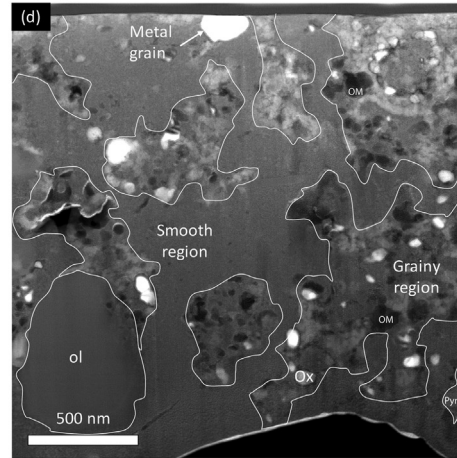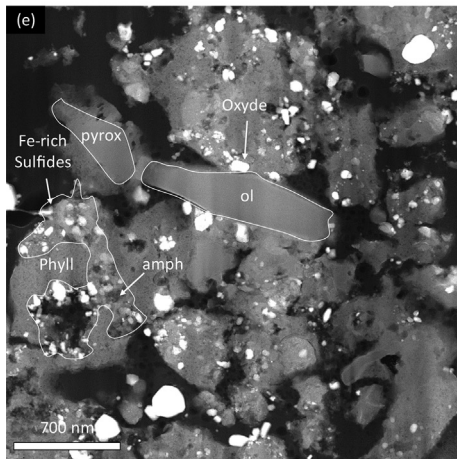
QUE 99177 (CR)
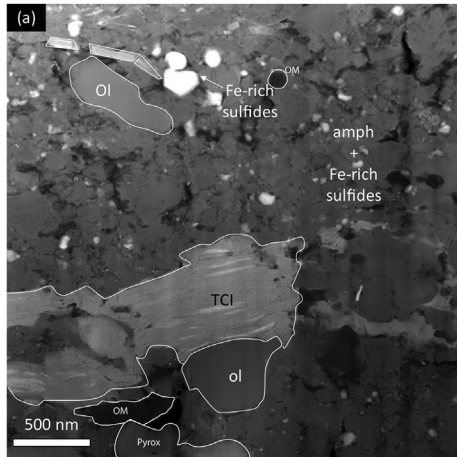
Matrix
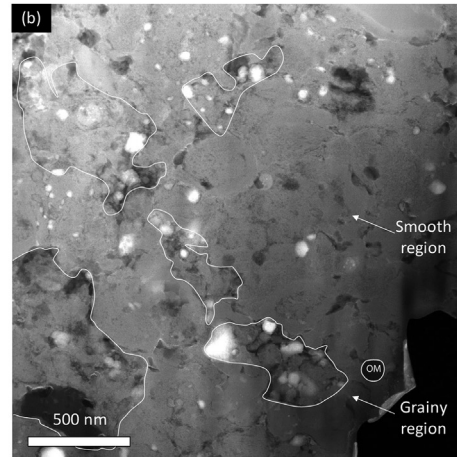
FGR

DOM 08006 (CO)
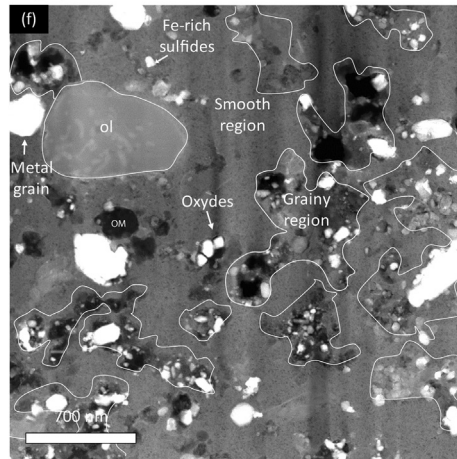

Matrix

FGR

Semarkona (LL)

Matrix

FGR

two types of textures "smooth" and "grainy". Grainy regions are similar to the matrix in terms of their metal and nanosulfide grain abundances and sizes.

In the CR chondrite QUE 99177, the porosity is low, both in the matrix and the FGRs (~4%). At the TEM scale few TCI are observed (~8 vol.%; Fig. 5 a). In the matrix, amorphous silicate domains are 400–500 nm in size. The nanosulfides in the matrix are distributed between 10 and 120 nm with a mean value of ~50 nm. In the FGR, the smooth areas are not continuous (unlike in DOM 08006 (CO) and Semarkona (LL)), and domains of 200–500 nm can be identified (Fig. 6 a). The distinction between the smooth and the grainy regions is difficult. Grainy regions are ~200 nm in size (Fig. 5 b). Sulfides, which are only present in the grainy regions have -at this scale- the same size distribution as in the matrix. Minor phases such as chromite, Ca-bearing pyroxenes, Fe-oxides, pentlandite, and Fe-oxide nanometric grains (20–100 nm) are found associated with the sulfides. These phases are in low abundance and were not observed by SEM since their size is inferior to 50 nm. Their presence does not affect the matrix composition.

In the CO chondrite DOM 08006, the two matrix FIB sections are comparable whereas the ones extracted from the two FGRs differ. Both matrix and FGRs contain sulfides mostly < 50 nm and metal grains of ~100 nm in size, showing heterogeneous Ni content (Fig. 5 c,d). Locally, parts of these metal grains are oxidized (Fig. 6 b). The matrix displays some porosity (8 vol.% - Fig. 5 c) and 2.1 % vol.% sulfides. Domains of amorphous silicate range from 100 to 500 nm. The FGR around the Type I chondrule (CO-Ch1) has a compact texture (porosity 2.8 vol. %; Fig. 5 d) and displays smooth regions that are particularly homogeneous and continuous. Grainy regions contain Fe-rich olivine (Fo_{60}) and olivine grains with a Mg-rich core (Fo_{95}) surrounded by Fe-rich rim (Fo_{60}) (Fig. 6 b). Their size ranges from 0.2 to 1 μm. The FGR associated with the Type II chondrule (CO-ch2) shows characteristics remarkably similar to its adjacent matrix at the TEM scale (Fig. S7) except that it does not contain large anhydrous silicates and sulfides (>5μm). Minor phases such as chromite, Mn-bearing olivine, pentlandite, apatite, Fe-rich olivine (Fo_5) and Ca-rich pyroxene are visible at the nanoscale.

The LL chondrite Semarkona also contains sulfide and metal grains mostly < 50 nm in both the matrix and the FGRs (Fig. 5 e,f), but metal grains are in lower abundance

than in DOM 08006 (CO) (Fig. 5 c,d). In the matrix, domains of amorphous silicate range from 100 to 600 nm in size and an abundant porosity is observed (20 vol.%, the highest of the three chondrites). Phyllosilicates are also observed (Fig. 5 e). FGRs are less porous (5.8 vol.%; Fig. 5 f). Grainy regions range from 0.1 to 1 μm in size. The smooth areas are nanocrystalline unlike those in DOM 08006 (CO) and QUE 99177 (CR) (Fig. 6 c). Minor phases in the FGR are chromite, carbonates and apatite.

3.5.2. Multi-layered FGR/coarse-grained rim

LL-ch2 displays a multilayered structure in contact with a porous matrix (Fig. 7 a). SEM images show an increase of the abundance and grain sizes of sulfides, olivine and pyroxene toward the chondrule from 4 vol.% in the outer part of the FGR to 34 vol.% close to the chondrule.

The matrix and FGRs assemblages (FIB 1 and 2) resemble the LL-ch1 sample described earlier (Fig. 5 e and f). FIB 3 has been sampled at the interface of the inner FGR and the outer FGR (Fig. 7 a). In the inner region, the nanocrystalline and chemically homogeneous silicate embeds coarse-grained anhydrous silicates, pentlandite and troilite assemblages (Fig. 7 b). The porosity is low (3 vol. %). The sulfide grains range between 100–150 nm. The FGR (outer rim) contains abundant metal grains (<100 nm) while they are absent in the coarse-grained rim (inner rim).

3.6. Compositions of amorphous and anhydrous silicates

3.6.1. Amorphous silicate average composition and water content

A phase map was obtained for each FIB section and the averaged composition of the amorphous silicate was extracted (Fig. 8 and Fig. S8, S9, S10 and Table S6). Amorphous silicate in FGRs (grainy and smooth averaged) and adjacent matrices have similar compositions. However, their compositions differ in the different chondrites. The amorphous silicate in Semarkona (LL) (which is nanocrystalline in smooth regions) has higher Si + Al value than in DOM 08006 (CO) and QUE 99177 (CR). The latter show higher values of Fe/Si (0.75 to 1.05 at.) in comparison to Paris (CM) (0.70 to 0.75 at.) and Semarkona (LL) (0.50 to 0.65 at.). DOM 08006 (CO) and QUE 99177 (CR) also exhibit similar Mg/Si values (0.35 to 0.55 at.). The LL chondrite Semarkona is characterized by the lowest Mg/Si values (0.25–0.4 at.) and the CM chondrite Paris the highest

---

Fig. 5. STEM-HAADF images of the FGRs and their adjacent matrix that surrounds the CR-ch1, CO-ch1, and LL-ch2 chondrules. In all chondrites, the matrix consists of a porous amorphous silicate enclosing anhydrous silicates (mainly Mg-rich olivine) and nanosulfides while the FGRs are more compact and divided into two characteristics regions (called "smooth" and "grainy", and marked by white lines). (a) The compact matrix of QUE 99177 (CR) is characterized by rare micrometer-sized TCI (b) The FGR of QUE 99177 (CR) consists essentially of amorphous silicate. The nanosulfides are heterogeneously distributed between the grainy and the smooth regions. (c) The matrix of DOM 08006 (CO) is porous. Numerous submicrometric grains of olivine, metal and Fe-oxides (magnetite) are present. (d) The associated FGR presents the most chemically homogeneous and continuous smooth regions. Grainy regions are porous and consist of amorphous silicate that embed nanosulfides, metal grains and small (<100 nm) Fe-rich olivines. (e) The matrix of Semarkona (LL) is highly porous. Small (50–100 nm) phyllosilicates sometimes surround the amorphous silicate domains. (f) The associated FGR (outer rim) display nanocrystalline smooth regions. Grainy regions are porous and consist of amorphous silicate that embed nanosulfides and metal grains. ol: olivine, pyrox: pyroxene, TCI: Tochilinite-Cronstedtite intergrowth, amph: (Fe-Mg) amorphous silicate, phyll:phyllosilicate, OM:organic material.
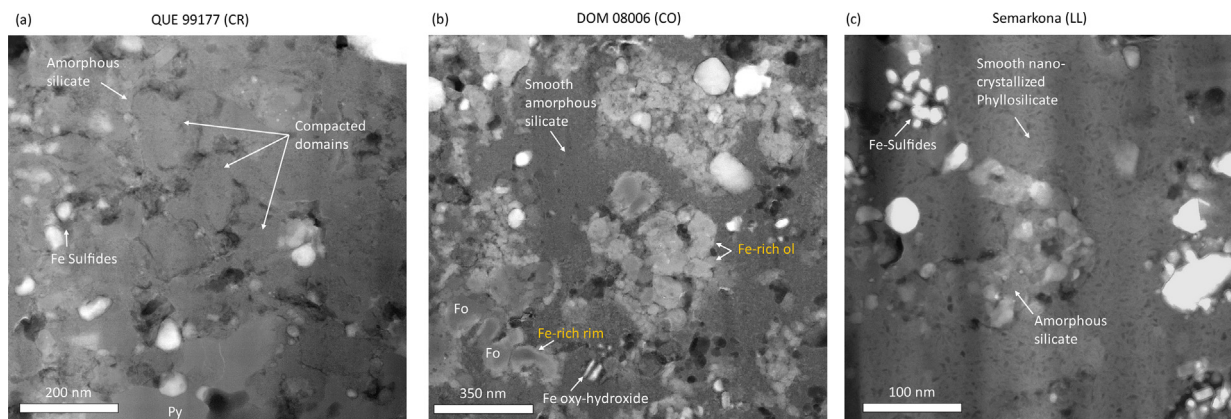
Fig. 6. Detailed STEM-HAADF image of the FGRs. (a) QUE 99177 (CR-ch1): compact and sulfide-free domains. b) DOM 08006 (CO-ch1): nanometer-sized olivines (Fe-rich and Mg-rich with fayalitic-rim). c) Semarkona (LL-ch1): smooth nanocrystalline phyllosilicates embedding amorphous silicate bearing sulfides and Fe-oxide grains. Fo = Forsterite, Ol = Olivine, Py = pyroxene, TCI = tochilinite-cronstedtite intergrowths.
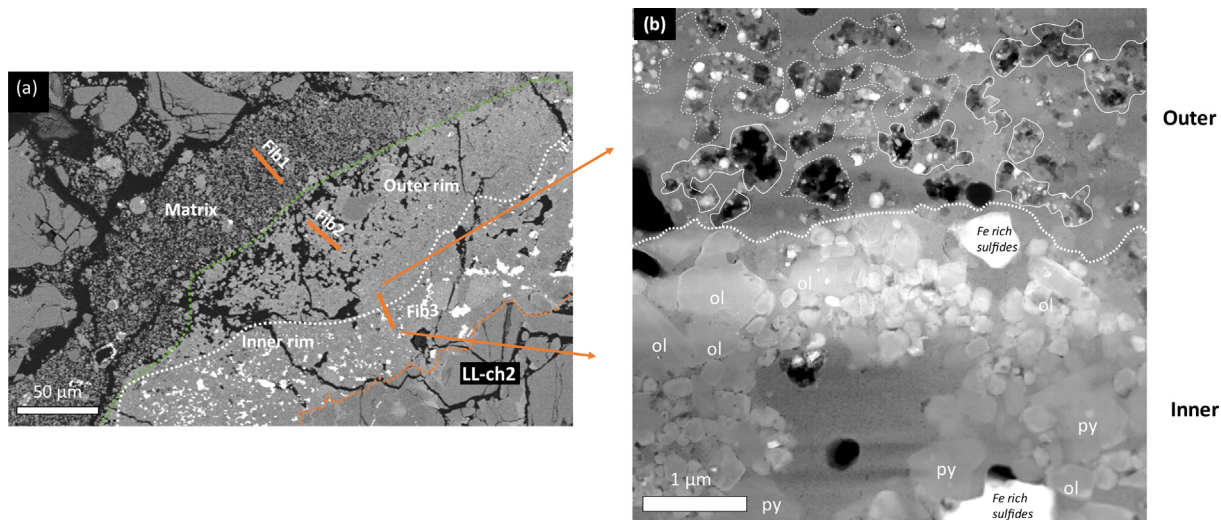

Fig. 7. (a) BSE image of the multilayered chondrule rim in Semarkona (LL). FIB 3 was extracted at the interface between the inner and the outer part. b) HAADF image of the targeted interface in the FIB 3 in Semarkona LL-ch2 chondrule. Larger grains of olivine and sulfides characterize the inner rim. The grainy regions are no longer visible in this area. ol: olivine, py: pyroxene.

(0.55–0.7 at.). Semarkona (LL) has the highest Na/Si (2–4 at.) and K/Si (2–6 at.) value. No correlation between Al + Ca and Na + K or other pair of elements was observed.

The water content of the amorphous silicate varies according to the chondrite (Fig. 9) but the values for the rim and the matrix within a given chondrite are similar to one another. DOM 08006 (CO) exhibits the lowest values (rim: 1.3% and matrix: 2.5%) while Paris (CM) shows the highest (rim: 6.8% and matrix: 6.5%). Semarkona (LL) and QUE 99177 (CR) are intermediate (rim: 4.6% and matrix: 4.1 % for the Semarkona (LL) and rim: 4.6% and matrix: 5.0% for QUE 99177 (CR)). The water content correlates with the S concentration in the amorphous silicate (sulfide nanograins were carefully excluded). A comparison to previous works is given in Table S7.

We also determined the anhydrous silicate compositions (Fig. S11) and found similar compositions in the matrices and the FGRs. The Mg# (Mg# = Mg/[Mg + Fe]) is between 0.5 and 1 for olivine and 0.7 and 1 for pyroxene. More than 80% of these silicates are forsterite and enstatite (i.e. Mg# > 0.92). Pyroxenes are generally poor in Al (Al/Si < 0.08) and in Ca (Ca/Si < 0.1).

3.6.2. Grainy vs smooth area compositions in FGRs

The smooth areas of amorphous silicate are chemically homogeneous and S-poor (Table S8) in all chondrites (Fig. 10 and Table S8). In contrast, the grainy regions exhibit variability mainly due to the mixing of amorphous silicate with nanophases (sulfides and Fe-oxides or sometimes metal grains for DOM 08006 (CO) and Semarkona (LL)). Fe-rich olivine (Fa_{60}) is intermingled at the nanos-
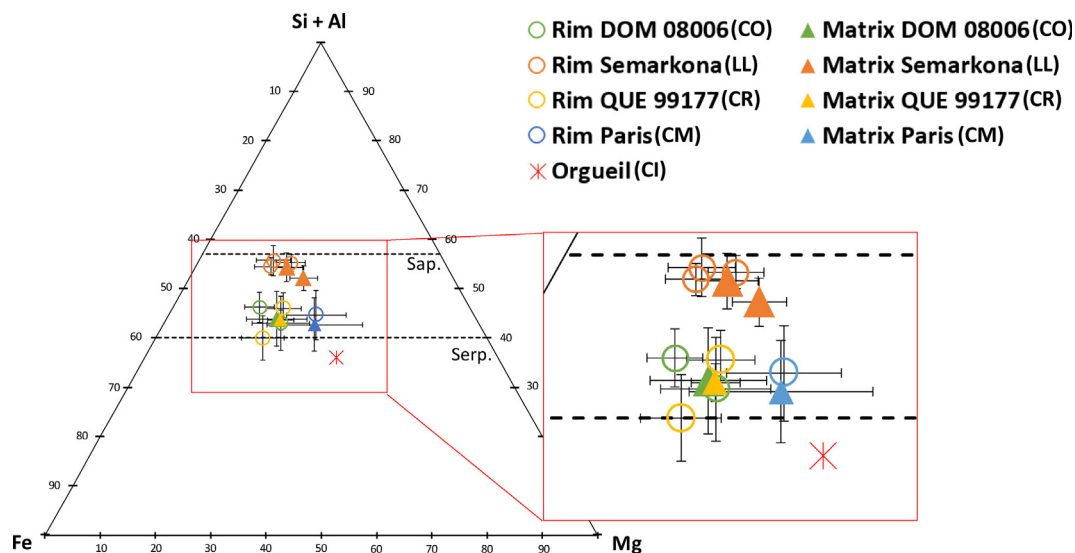
Fig. 8. Ternary Fe-Mg-Si + Al diagram (at.) showing the average composition of the amorphous silicate (also includes nanocrystallized phyllosilicates in the case of Semarkona (LL)). The bulk composition of Orgueil (CI) is given as reference (Lodders, 2010). Data from Paris (CM), obtained using the same methodology, are also included (Zanetta et al., 2021). Horizontal lines represent the saponite and serpentine solid solutions, sap: saponite, serp: serpentine.
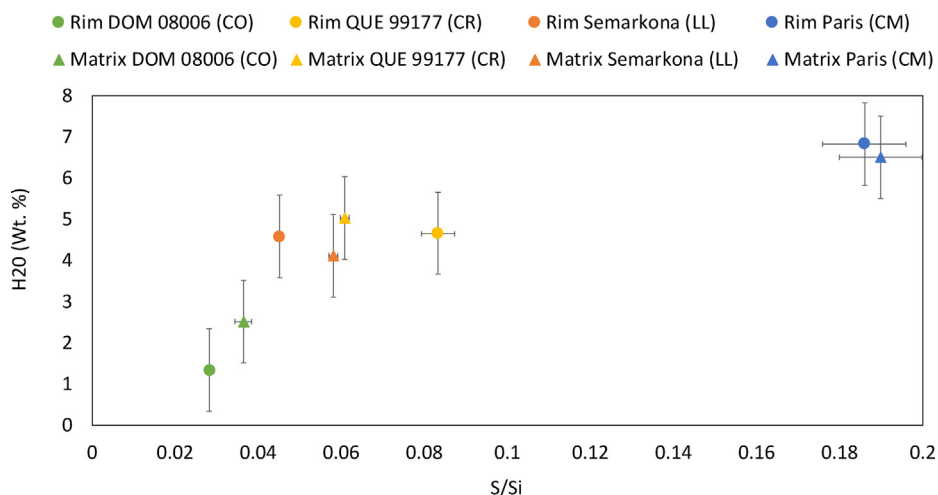

Fig. 9. H_2O content in the amorphous silicate/phyllosilicate cementing the material in the different FIB sections. The H_2O content is plotted as function of S/Si (at.). Averaged values are obtained from a pixel selection using the phase map. S-rich pixels are avoided to minimize mixing with nanosulfide grains. The water content is derived from the OH content which is calculated by stoichiometry to obtain charge neutrality. Paris is added for CM comparison.

cale with the amorphous silicate in the grainy regions of DOM 08006 (CO) (Fig. 10, as in Fig. 6 b).

The smooth regions of the outer rim of the LL-ch2 are similar to the LL-ch1 FGR, i.e. they are chemically homogeneous while grainy regions exhibit a much wider composition range due to the mixing with nanophases (Fig. 11 a). The composition field of the phyllosilicates (red triangles) in the inner coarse-grained rim (Fig. 11 b) is narrow and resembles the composition field of the smooth regions in the FGRs of the LL-ch1 and LL-ch2 (outer rim) chondrules. The material is, however, poorer in Fe and more hydrated. The coarse-grained regions contain Ca-pyroxene, Mg-rich pyroxene (En_{90-100}), Mg-rich olivine

(Fo_{60-90}) and large sulfide (pentlandite and troilite) grains that are embedded in the nanocrystalline phyllosilicate. Some Mg-rich olivine grains show clear Fe-rich rims at their boundary.

4. DISCUSSION

4.1. Thermally processed FGRs, similarities with the Paris chondrite

4.1.1. Aqueous alteration is unlikely to generate FGRs

Previous studies showed that the meteorites we selected for this study are amongst the most primitive chondrites
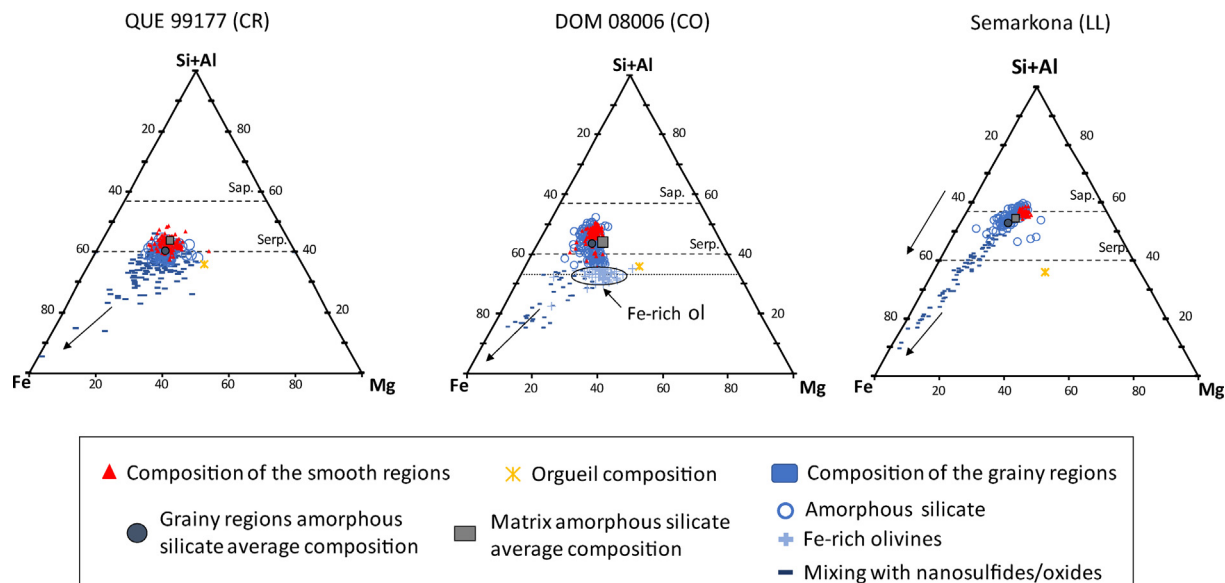
Fig. 10. Fe, Mg, Si + Al ternary diagrams showing the composition fields of the FGR sampled in the three chondrites (at%). Data are extracted from regions of interest in the smooth and grainy areas (i.e from CR-ch1, CO-ch1 and LL-ch1 areas). Quantified pixel size is between 15 and 25 nm. Diagrams consist of 200 points per regions. The red triangles represent the quantified pixels from the smooth regions. The blue markers represent the compositions from the grainy regions. Grainy regions are subdivided into three markers (circles, crosses and hyphens) to represent the constituents (i.e. amorphous silicate, Fe-rich olivines and amorphous silicates mixed with nanosulfides/oxides respectively). The average composition of matrix amorphous silicate (gray square) is close to the smooth amorphous silicate composition and to the average of pure amorphous silicate pixels from grainy regions (dark circle).Orgueil bulk composition is given as a comparison (Lodders, 2010). Sap: saponite, serp: serpentine. The two horizontal dashed lines represent the saponite and serpentine solid solution. The dotted line represents the olivine solid solution.

(Floss and Stadermann, 2009; Abreu and Brearley, 2010; Nguyen et al., 2010; Harju et al., 2014; Bonal et al., 2016; Nittler et al., 2018; Quirico et al., 2018; Dobrică et al., 2019; Davidson et al., 2019). Several lines of evidence confirm that only limited parent body aqueous alteration affected the matrices and FGRs: 1) The abundance of amorphous silicate, because it is metastable and would rapidly form phyllosilicates (Rietmeijer et al., 2004; Chizmadia and Brearley, 2008; Nakamura-Messenger et al., 2011; Le Guillou et al., 2015b; Leroux et al., 2015); 2) the limited size of sulfides (<50 nm) since sulfur is mobile and sulfides would easily form larger grains (Greshake, 1997; Chizmadia and Brearley, 2008; Abreu and Brearley, 2010; Le Guillou and Brearley, 2014; Davidson et al., 2019); 3) the absence of metal oxidation in contact with amorphous silicate, since it is also expected to be amongst the first alteration reaction to occur (Brearley, 2006).

Even though the aqueous alteration was limited, it impacted each of the three chondrites to some extent. In QUE 99177 (CR), Fe-oxides, TCI and nanocrystalline phyllosilicates are found in the matrix and in the rims. TCIs are characteristic species of the first stages of alteration and form under low temperature conditions (Rubin et al., 2007; Harju et al., 2014; Pignatelli et al., 2017). In Semarkona (LL), the presence of phyllosilicates in the matrix and nanocrystalline phyllosilicates in the rims (Fig. 5 e, f and Fig. 6 c) also indicates some degree of aqueous alteration. In the rim, they replaced the smooth regions. In DOM 08006 (CO), Fe-oxides have replaced part of the metal grains, indicating oxidizing conditions and likely due to par-

ent body alteration. However, in the three chondrites, no matter the degree of alteration, FGRs and matrix have been affected in a similar way. This is consistent with the water content of the amorphous silicate (Fig. 9) which is similar in the matrix and in the rims. We conclude that a secondary parent body process cannot explain the specific characteristics observed in FGRs and is hence unlikely to have generated them. Instead, a nebular accretion is favored.

4.1.2. Nature of the dust reservoirs and FGR thermal processing

The fine-grained material that made up FGRs and matrices exhibits mineralogical and chemical similarities. The same phases are observed (anhydrous silicates, nanosulfides, nano-Fe-oxides and metal) and the size distribution of the finer grained population (nanosulfides and the anhydrous silicates < 4 μm) is similar. Their compositions, both at the SEM scale (Fig. 4 a) and at the TEM scale (amorphous silicate Fig. 8) are similar to one another. We thus conclude that in a given chondrite group, FGRs and matrix originated from a common dust reservoir. However, their compositions differ according to the chondrite group and differ from CI (Fig. 4 a). The amorphous silicate (that is the primary component of the fine-grained material) composition is characteristic of the chondrite (Fig. 8) and suggest that each chondrite sampled a different dust reservoir. This affects the chondrite bulk compositions. For instance, the enrichment in Si, K and Na in the fine-grained material (Fig. 4 a and Fig. 8) observed in the LL chondrite Semarkona in comparison to the other chondrites
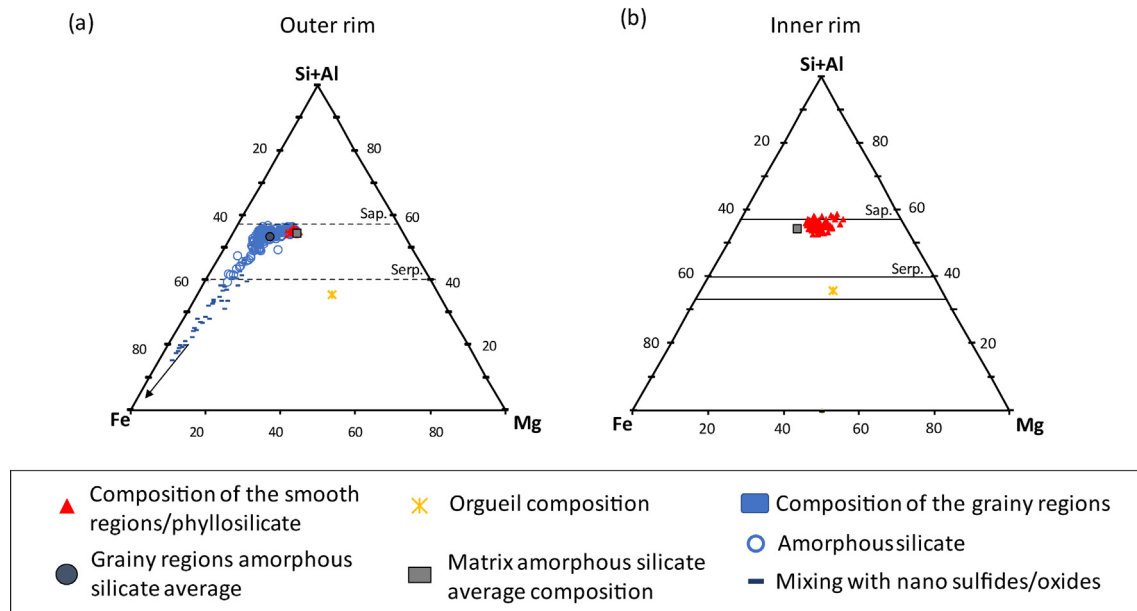
Semarkona LL-ch2 chondrule

Fig. 11. Fe, Mg, Si + Al ternary diagrams (at. %) showing the composition of the FGR and the coarse-grained rim that surround the LL-ch2 chondrule in the Semarkona chondrite (see Fig. 7 b). a) Data represent the quantified pixels extracted from the grainy (blue markers) and smooth (red triangles) regions in the outer rim. Grainy regions are subdivided into different shaped markers to represent the constituents (i.e. amorphous silicate and amorphous silicates mixed with nanosulfides/oxides respectively). The average composition of matrix amorphous silicate (gray square) is close to the smooth amorphous silicate composition. In comparison, the average composition of pure amorphous silicate pixels from grainy regions (dark circle) is more Fe-rich and Mg-poor. Quantified pixel size is 17 nm. The diagram consists of 200 points per region. b) For the inner rim, only the phyllosilicate composition (red triangles) that embeds the large (>200 nm) anhydrous silicates and sulfide grains in the Fig. 7 b (inner rim) is plotted. There is no amorphous silicate in the inner rim. The average composition of matrix amorphous silicate (gray square) is more Fe-rich than the phyllosilicate in the smooth region (red triangles). The anhydrous silicate and sulfide grains are not represented here. Orgueil bulk composition is given as a comparison point (Lodders, 2010). The two horizontal dashed lines represent the saponite and serpentine solid solutions. Quantified pixel size is 15 nm. The diagram consists of 300 points (narrow composition field). Sap: saponite, serp: serpentine.

we studied is characteristic of the ordinary chondrites (Scott and Krot, 2014).

Despite the chemical/mineralogical similarities between matrices and FGRs, they each also exhibit their own characteristics. (1) In all samples, FGRs are characterized by a porosity lower than that of the matrix. In the case of DOM 08006 (CO) and Semarkona (LL) this difference is clear (Fig. 5; 2.8% vs. 8% and 5.8% vs. 20%, respectively). In the CR chondrite QUE 99177 the difference is not as big, possibly because of the filling of the matrix porosity by secondary phases (TCIs Fig. 6 a). Based on the abundance of TCIs (low in the FGRs) we infer that the porosity was also initially higher in the matrix than in the FGR (12 % vs. 4% if TCIs are removed). (2) Matrices also encompass a coarse-grained population (>4μm) of anhydrous silicates (Fig. 2, Fig. 3, Table 3 and Fig. S5, S6) that we described as a dichotomy in size-distribution. Based on results obtained on the CM Paris chondrite, Zanetta et al. (2021), proposed that the reservoir yielding to the FGRs and the matrix initially contained small (<4μm) anhydrous silicates and that the larger population, which is only observed in the matrix is the result of a chondrule fragmentation episode (Alexander et al., 1989a, 1989b). (3) FGRs

are heterogeneous. They contain extended areas of smooth and chemically homogenous amorphous silicate that surround granular pockets rich in Fe-oxides and nanosulfides (Figs. 5 and 6). The grainy regions are similar to what is found in the matrix. These characteristics have already been observed in the Paris CM (2.7–2.9) chondrite (Zanetta et al., 2021) as well as in the CM2 chondrite Y 791198 (Chizmadia and Brearley, 2008). Recently, Vollmer et al., (2020) also noticed comparable textures in two CR2 chondrites (MIL07525 and GRA95229) with smooth amorphous texture interrupted by sulfide-rich areas.

The fact that FGRs share chemical and mineralogical similarities with their matrices in any given chondrite we studied, suggests that the same dust reservoir generated the matrix and FGRs. However, the dust accreted onto chondrules (i.e., forming FGRs) was likely transformed in the nebula giving the FGRs their own characteristics. The matrix escaped this transformation and was accreted later, together with isolated large sulfides and anhydrous silicates grains that are probably chondrules fragments (Alexander et al., 1989a, 1989b). In the Paris CM chondrite, Zanetta et al. (2021) suggested that a thermal modification in a nebular setting (i.e. before incorporation into the parent body)
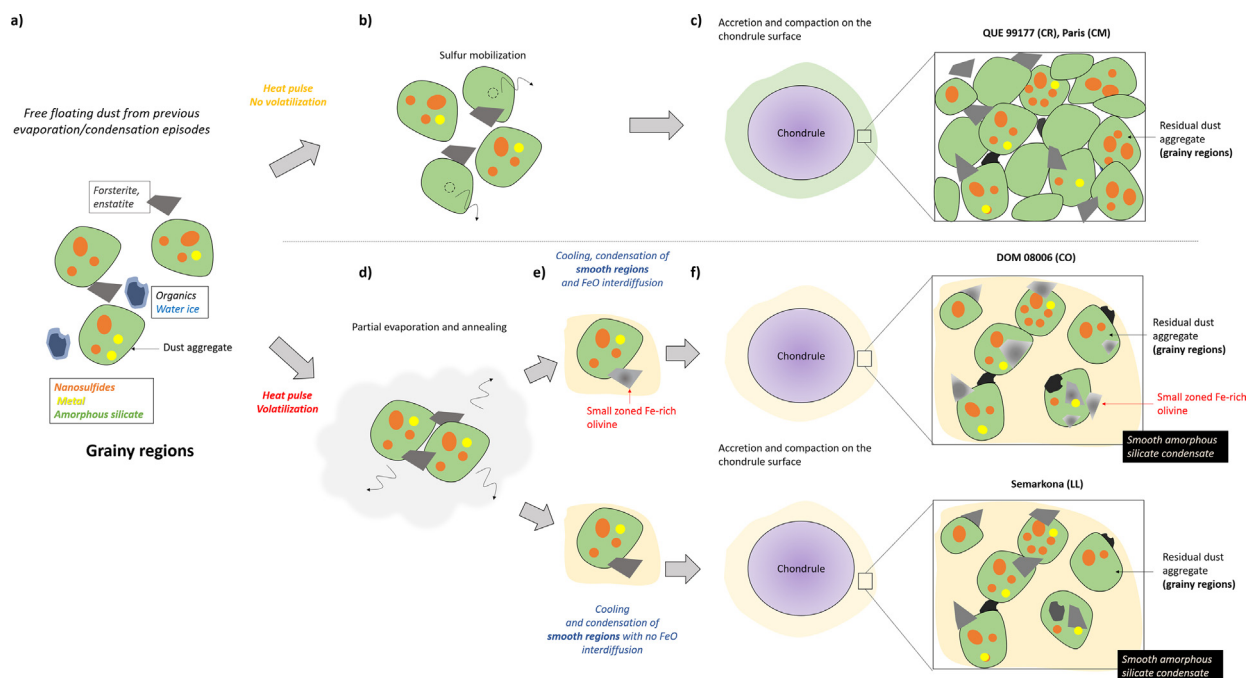
Fig. 12. Proposed scenario for the formation of the grainy and smooth regions in FGRs. Multiple evaporation events might have processed dust populations at different times and at various temperatures. Grainy regions are formed prior to the smooth silicate condensate, in the same region or during a previous episode. Depending on the conditions (T, fO$_2$, FeO concentration, density of dust) the intensity of the transformation varies. All FGRs have been subjected to a heat pulse and compacted onto the chondrule surface. a) Reservoir of free floating dust parental to the grainy regions (amorphous silicate bearing nano-sulfides) observed in the FGRs and the matrix. Green: amorphous silicates, orange: nano-sulfides, yellow: metal, gray Mg-rich anhydrous silicates (pyroxene and olivine), blue: water ice surroundings dark: organics. The assemblage is thermally processed by a heat pulse (b,d). b) In QUE 99177 (CR) and Paris (CM), the heat pulse mobilizes the sulfides, leading to a progressive removal of nano-sulfides initially present in the amorphous silicate. c) the weakly processed assemblage is compacted on the surface of the chondrules. d) The heat pulse partially volatilizes the initial dust reservoir in a). e) In DOM 08006 (CO) and Semarkona (LL) after the heat pulse the gas cooled which favored the condensation of smooth amorphous silicates (beige) around the remaining-unvolatilized- grainy regions. In DOM 08006 (CO) the high temperature (>800 K) induced the interdiffusion of iron coming from the amorphous silicate to the Mg-rich anhydrous silicates (gradient fill). In Semarkona (LL) the smooth silicate encloses the grainy regions, but the conditions were not propitious to the formation of Fe-rich olivine (solid fill). f) The assemblage is compacted onto the chondrules. The dark regions represent the organics after the volatilization of the water during the heat pulse. The empty spaces represent the porosity.

transformed the dust and favored its compaction onto the chondrules, giving the FGRs their own characteristics. We propose that the following are additional arguments in favor of a thermal modification of the nebular dust prior to its accretion onto chondrules to form FGRs: the compaction and the modification of the microtexture; the sulfide mobilization that led to sulfide-free amorphous silicate domains in Paris (CM) and QUE 99177 (CR); the smooth silicates that enclose grainy regions and that are present in the FGRs of DOM 08006 (CO) and Semarkona (LL) but not in the matrices (likely resulting from an evaporation/condensation process); and perhaps the Fe-rich olivine in DOM 08006 (CO). These arguments are discussed in the following section.

Given the similarities of the micro-texture between the FGRs of the three newly described chondrites, Y 791198 (CM) described by Chizmadia and Brearley, (2008), MIL07525 (CR) and GRA95229 (CR) described by Vollmer et al., (2020) and the Paris CM chondrite (Zanetta et al., 2021) it is likely that a similar process affected all chondrite groups (to different extents) independently of their location and time formation. We suggest

that the thermal process advocated for the transformation of the dust in the nebula and producing FGRs is ubiquitous and must be considered alongside the chondrule and matrix formation process. This could also help to shed light on the genetic relationship between chondrite components.

4.2. Mechanisms and temperature of FGRs processing

4.2.1. Variable temperatures of FGR processing

FGRs in Paris (CM) and QUE 99177 (CR) appear to be less processed than in Semarkona (LL) and DOM 08006 (CO) (Fig. 12). In the former two, grainy and smooth regions are more difficult to distinguish than in the latter two, and the matrix also looks more similar to the FGRs (Fig. 5 a,b – Fig. 6 a and (Zanetta et al., 2021)). Furthermore, smooth areas form delimited domains in QUE 99177 (CR) and Paris (CM) chondrites (Fig. 5 a,b and Fig. 6 a), whereas they are continuous over hundreds of nanometers in DOM 08006 (CO) and Semarkona (LL) (Fig. 5 c,d,e,f and Fig. 6 b,c). These microstructures reveal dissimilar intensity of the thermal modification that the FGRs experienced.

The chondrites Paris (CM) and QUE 99177 (CR) exhibit a similar FGR micro-texture with delimited amorphous silicates domains without any nano-sulfides juxtaposed with grainy regions (i.e., amorphous silicates domains bearing nano-sulfides). Zanetta et al., (2021) suggested that it was the result of a minor sulfide mobilization (Fig. 6 a and Fig. 10 a) and constrained the maximum temperature reached by FGRs to be lower than 800 K. We also suggest that smooth and grainy regions found in the FGRs of these chondrites formed through a heat pulse in the nebula. The initial reservoir of free-floating dust that became the grainy regions was partially affected by this thermal process and part of the nano-sulfides were volatilized leading to the formation of domains of amorphous silicate free of sulfides. The smooth and grainy regions later accreted and compacted onto chondrules (Fig. 12 a,b,c).

In the CO chondrite DOM 08006, the smooth and chemically homogeneous amorphous silicate encloses the grainy regions (Fig. 6 b and Fig. 10 b). How did the smooth amorphous silicate form and is it related to the amorphous silicate found both in the matrix and in the grainy regions? Given that the water content of these amorphous silicates is low in comparison to the other chondrites (Fig. 9 and Table S7) and that other evidence of aqueous alteration is absent, we exclude the possibility that the smooth amorphous silicate could be the result of the parent body alteration of an original population of nanosulfide-bearing amorphous silicate. The main astrophysical processes that have been proposed to form amorphous materials are disequilibrium condensation, particle irradiation, shock amorphization, and rapid cooling of melts (Nuth et al., 2005). The favored scenario invokes an origin by dust evaporation followed by rapid, disequilibrium condensation (nucleation of crystalline silicate phases is inhibited, e.g., (Stephens and Kothari, 1978; Nuth and Donn, 1983; Brearley, 1993; Rietmeijer et al., 1999; Nuth et al., 2000, 2002, 2005)). In terms of astrophysical settings, the chondrule-forming event is the favored candidate (short duration, high temperature, rapid cooling) (Lewis et al., 1993; Nagahara et al., 1994; Kita et al., 2000; Huss et al., 2003; Nuth et al., 2005; Libourel and Chaussidon, 2011; Desch et al., 2012; Marrocchi and Chaussidon, 2015). Previous authors suggested that during chondrule-forming events, the mass of solids vaporized was likely significant (or about the same) in comparison to the mass that melted to form chondrules and should recondense during subsequent cooling (Brearley, 1993; Wasson, 1996). Following previous studies, we also suggest that spatial variations of maximum temperatures and cooling rates around the chondrule-forming region can lead the same mechanism to form different type of materials (i.e., rapidly cooled amorphous silicate and slower-cooling chondrules). We therefore propose that the smooth regions are condensates originating from a dust evaporation/condensation episode (Fig. 12 a,d,e). The sulfide/oxide-bearing amorphous silicate found in the matrix and in the grainy regions likely originated from a previous dust evaporation episode. However, the smooth regions could also have formed during the same episode (and in the same reservoir) than the amorphous silicate found in the matrix and in the grainy regions but in a higher temperature region and experienced different cooling conditions. In both scenarios, the smooth amorphous silicate evaporates at a different temperature than the other amorphous silicates (grainy regions and matrix), since it lacks sulfides and Fe-oxides, and condensed later to enclose the grainy regions. The dust assemblage then accreted and compacted onto the chondrule surfaces (Fig. 12).

The grainy regions of CO chondrite DOM 08006 contain characteristic small Fe-rich olivine grains intermingled with the amorphous silicate (Fig. 6 b and Fig. 10 b). Such Fe-rich olivine is rare in pristine carbonaceous chondrites and chondritic porous interplanetary dust particles which are dominated by Mg-rich silicates instead (Brearley, 1993; Greshake, 1997; Keller and Messenger, 2011; Leroux et al., 2015). These Fe-rich olivine grains in the FGRs are different from those observed in the matrix. They are much smaller and have Mg-rich cores (Fo_{97}) and Fe-rich rims (Fo_{44}). In contrast to Fe-rich olivine in the matrix, the Fe content is not correlated to the Mn content (Fig. S12). This indicates that they are not fragments of Type II chondrules like the ferroan olivine grains in the matrix (Miyamoto et al., 1993; Goodrich and Delaney, 2000; Papike et al., 2003; Berlin et al., 2011). Their presence therefore holds valuable information about the temperature experienced by the grainy regions. They appear to have replaced or grown from previously existing micrometer-sized Mg-rich olivine (Fig. 6 b). Two mechanisms might explain their formation: 1) interdiffusion of iron coming from the amorphous silicate into pre-existing Mg-rich olivine (Housley and Cirlin, 1983; Kojima and Tomeoka, 1996; Krot et al., 1997b; Krot et al., 1998; Brearley, 1999; Imai and Yurimoto, 2003; Krot et al., 2004b; Howard et al., 2010; Cuvillier et al., 2015); 2) solid–gas interaction where Mg-rich olivine grains reacted with the gas produced by the evaporation of the dust (MacPherson et al., 1985; Peck and Wood, 1987; Hua et al., 1988; Palme and Fegley Jr, 1990; Weinbruch et al., 1990; Weinbruch et al., 1993; Murakami and Ikeda, 1994; Weisberg et al., 2006; Nozawa et al., 2009; Varela et al., 2012). However, previous authors have shown that even under oxidizing nebular conditions (fO_2 a hundred times greater than the canonical value) with elevated dust to gas ratios, it is not possible to form Fe-rich olivine with a mole fraction of fayalite (XFa) > 0.145 (Fedkin and Grossman, 2006; Dobrică and Brearley, 2020b). Additionally, if the individual phases of the grainy regions were already assembled (Mg-rich olivine, amorphous silicate and sulfides/Fe-oxides) when the Fe-rich olivine formed, then the temperature was certainly higher than 800 K for the Fe to diffuse into the Mg-rich olivine but lower than ~1000 K to preserve the amorphous silicate (Murata et al., 2007). Such temperatures are given as estimations, but they may significantly change as function of the duration of the heat pulse, the pressure, the oxygen fugacity and the Fe and Mg concentration in the amorphous silicate (Fig. 12 d). Ultimately, the condensation of the smooth amorphous silicate would have occurred at lower temperature around the residual grainy regions containing Fe-rich olivine (Fig. 12 e). The dust then accreted onto chondrules (Fig. 12 f).

In the LL chondrite Semarkona, the FGRs do contain smooth regions (Fig. 6 c and Fig. 10 c), which indicates that, at some point, the evaporation temperature of the dust was reached, and condensation followed, embedding grainy regions (Fig. 12 a, d, e). However, smooth regions are not amorphous as in the CO chondrite DOM 08006 but are instead made of nanocrystalline phyllosilicates. Secondary alteration that occurred in the parent body is manifest in the matrix, where phyllosilicates are also observed (section 4.1.1; Hutchison et al., 1987; Alexander et al., 1989a, 1989b; Dobrică et al., 2019; Dobrică and Brearley, 2020a). Nanocrystalline phyllosilicates in the FGRs potentially formed by aqueous alteration on the parent body of the LL chondrite Semarkona (Fig. 13). An alternative would be that nanocrystalline phyllosilicates formed directly by condensation. However, this would imply a significant input of water to the gas at the time of condensation in order to reach a high partial pressure of water (Ciesla et al., 2003). Another difference with DOM 08006 (CO) is that there is no fine-grained Fe-rich olivine with Mg/Fe zonation in the grainy regions, which only contain Fe-oxides, nanosulfides and Mg-rich anhydrous silicates in addition to the amorphous silicate (Fig. 6 c and Fig. 12 e). Grainy regions were likely subjected to lower temperature than in the CO chondrite DOM 08006, i.e. below the fayalitic olivine stability field, and/or placed in higher oxygen fugacity conditions that favored Fe-oxides rather than Fe-rich olivine (Zolotov et al., 2006).

4.2.2. Igneous rims as extreme cases of thermal processing

The LL-ch2 rim exhibits two layers with distinct textures. The inner rim texture (Fig. 1 f, Fig. 7 and Fig. 11) shares similarities with igneous rims observed in several types of chondrites with euhedral anhydrous silicates that comprise low Ca-pyroxenes (see 3.5.2.) and sulfides larger than in FGRs (Krot and Wasson, 1995). Mafic silicates and sulfides display small ranges in grain sizes. This suggests that the inner rim has been modified at higher temperature (T > 1000 K) than the outer rim. The outer rim is similar to the other FGRs found in the LL chondrite
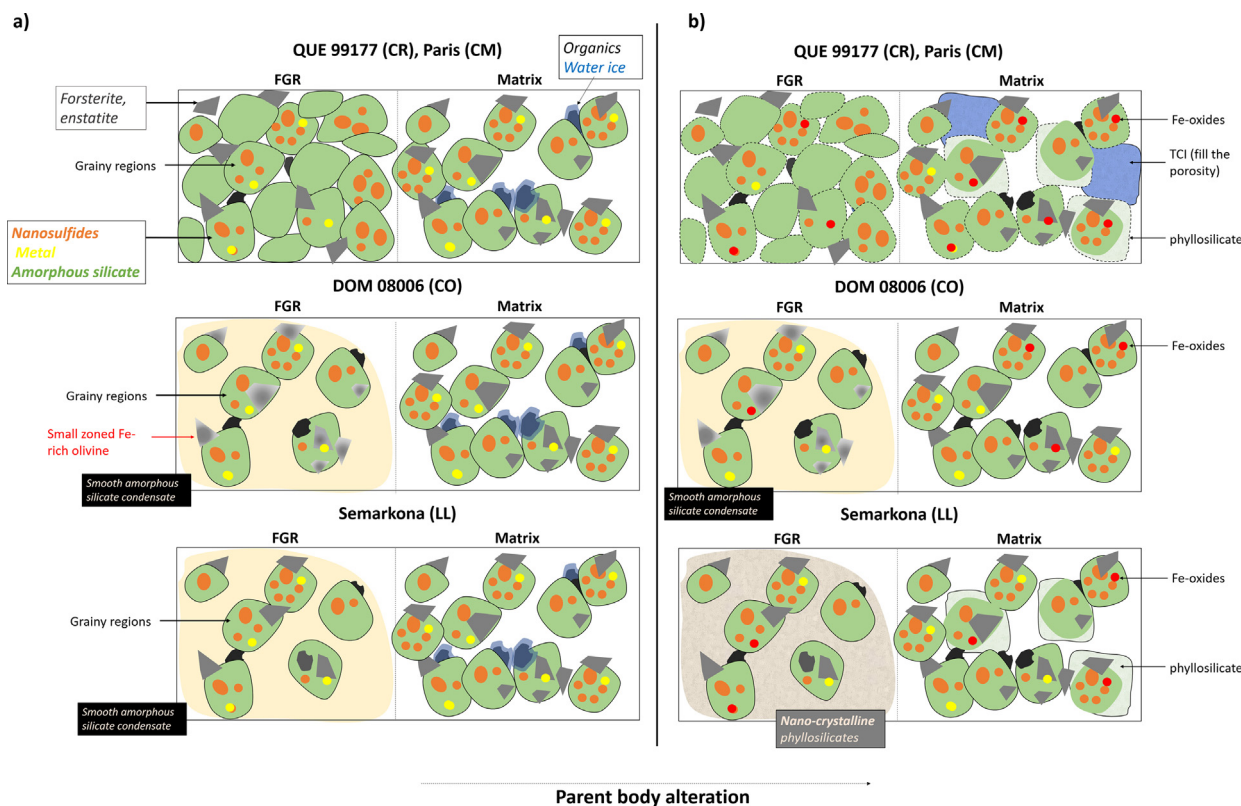

Fig. 13. Accretion of the matrix material and effect of the parent body aqueous alteration on the FGR and matrix micro-texture. a) The FGR material of Fig. 12 is shown alongside a porous matrix. The color key is as in Fig. 12: Green: amorphous silicates, orange: nanosulfides, yellow: metal, gray Mg-rich anhydrous silicates (pyroxene and olivine), blue: water ice surrounding dark: organics b) The aqueous alteration had a different impact depending on the component (FGRs or matrix) and the chondrite. In QUE 99177 (CR) and Paris (CM), the contours of the amorphous silicate domains are more difficult to distinguish in the FGR and in the matrix. In the latter, phyllosilicates and TCI patches filled the porosity. Most of the metal grains oxidized. In DOM 08006 (CO), the aqueous alteration impacted the microstructure to a limited extent, with the absence of abundant phyllosilicates and an open porosity still visible. Fe-oxides potentially formed on the parent body. In Semarkona (LL), the highly reactive smooth amorphous silicate in the rim transformed to nanocrystalline phyllosilicate. The amorphous silicate of the grainy regions remains unchanged. Fe-oxides formed during the alteration. In the matrix, the formation of phyllosilicate surrounding the amorphous silicate domains and Fe-oxides is observed.

Semarkona with the presence of smooth and grainy regions which suggests that it formed at lower temperature than the inner rim.

Krot and Wasson (1995) proposed that igneous rims are formed by partial melting and/or by direct condensation of a dust-aggregate (matrix-like) material and suggested that a continuum in properties existed between largely melted and unmelted rims. We have shown that the phyllosilicate of the inner rim has a composition that is similar to the amorphous silicate of the outer rim and to the matrix (Fig. 8, Fig. 11 and Fig. S9, S10 and Table S6) except that it is poorer in Fe and more hydrated. This suggests that FGRs and igneous rims could form from a similar precursor but at different temperatures. This hypothesis is supported by the abundances of igneous rims in comparison to FGRs. The relative abundances of igneous rims and FGRs have been observed to depend on the chondrite group (Rubin, 1984; Metzler et al., 1992; Metzler, 2004; McCanta et al., 2008; Krot et al., 2014; Scott and Krot, 2014; Krot et al., 2017). Igneous rims are common (26–50%) in CV, OC, CR, CK, CH, but are not abundant in CM or CO chondrites (Rubin, 1984; Metzler et al., 1992; Metzler, 2004; McCanta et al., 2008; Krot et al., 2014; Scott and Krot, 2014; Krot et al., 2017). Rubin (2010) estimated that igneous rims surround ~50% of the chondrules in CV3 chondrites, ~10% in H-L-LL3 chondrites, and < 1%, in CO3 chondrites. In comparison, we showed that the percentage of FGRs was constant once chondrule fragments were withdrawn from the statistics (~80%) while igneous rims was more abundant in QUE 99177 (CR) (8%) and Semarkona (LL) (20%) than in DOM 08006 (CO) (3%) and were not detected in Paris (CM) (Table 2). Thus, FGRs are relatively ubiquitous while igneous rims are more abundant in chondrites that experienced higher temperatures at the time of rim accretion.

It has been proposed that the heat source responsible for heating the igneous rims to T > 1400 K is the same one responsible for melting the chondrules (Krot and Wasson, 1995). We also proposed that the smooth and grainy regions were formed in the vicinity of the chondrule formation area. Additionally, we showed that the composition of the smooth silicate is similar in both rims (inner and outer) and that it is similar to the amorphous silicate of the matrix (Figs. 8, 10, and 11). We conclude that FGRs and igneous rims could have formed from a single reservoir but were thermally processed at various temperatures in the vicinity of the chondrule formation area (Krot and Wasson, 1995).

4.3. Astrophysical settings of FGR formation

4.3.1. the role of the local dust densities

It is generally accepted that chondrules formed in a dust-rich environment favorable for transient heating episodes at high gas partial pressure (Lewis et al., 1993; Nagahara et al., 1994; Kita et al., 2000; Huss et al., 2003; Libourel and Chaussidon, 2011; Desch et al., 2012; Marrocchi and Chaussidon, 2015). Alexander et al., (2008) proposed that several chondrule characteristics were controlled by local dust densities at the time of their formation. We present

here several insights suggesting that rims (FGRs and igneous rims) thermal modification could be associated with chondrule formation and controlled by the local dust density.

1) Chondrule sizes and igneous rim proportions appear to be correlated (Table 2 and Table S1). QUE 99177 (CR) and Semarkona (LL) have the largest chondrules and the lowest matrix abundances. These two chondrites also have the highest proportions of igneous rims around Type I chondrules (Table 2). In comparison to these chondrites, Paris (CM) and DOM 08006 (CO) exhibit smaller chondrules, and a lower abundance of igneous rims around Type I chondrules. Mechanisms that control the final chondrule size are debated (Metzler et al., 2019). Their size may be inherited from the chondrule-forming process itself (Kadono et al., 2008; Jacquet, 2014; Johansen et al., 2015), may also be inherited from the size of the precursors, or even result from a size-sorting process (Dominik and Tielens, 1997; Jacquet, 2014). Rubin (2010) suggested that the chondrule size might be controlled by the local density of dust. A higher density increases the interaction between the dust and the molten chondrule. It also enhances chondrule coalescence and favors larger chondrule size. Correspondingly, higher densities may imply higher local temperature. If chondrule sizes are controlled by the dust density, this may explain why a higher proportion of rims that were processed at higher temperature (i.e. igneous rims) is found in the chondrites that contain larger chondrules (Table 2). It is also possible that in the regions where high enough temperatures are reached to form igneous rims, part of the dust might be completely recycled, melted and formed into larger chondrules. This would also explain why igneous rims are more abundant in chondrite exhibiting larger chondrule size (Matsumoto et al., 2019).

2) In the CO chondrite DOM 08006 the FGR around the CO-ch2 Type II chondrule resemble the matrix (and the dust aggregate precursor material in Fig. 12) and does not exhibit any smooth and grainy regions. In contrast, the rim around the CO-ch1 Type I chondrule was thermally processed (see section 4.2.1). In the LL chondrite Semarkona, rims around Type I chondrules appear to be processed at higher temperatures (LL-ch2 inner rim). Krot and Wasson, (1995), showed that most of the igneous rims around low-Fe0 chondrules are significantly melted while the degree of melting is commonly less in rims around FeO-rich chondrules. They estimated a formation temperature of 1840 K for low FeO chondrule igneous rims and 1700 K for high-Fe0 chondrule igneous rims. (Tenner et al., 2013, 2015) showed that Type I and Type II chondrules formed in reservoirs differing in dust and ice content, for both the CO and CR chondrites. Alexander et al., (2008) suggested that Type I and Type II chondrule characteristics are influenced by the density and the composition of the dust. Thermodynamic calculations show that for a given temperature, the density of solids required to retain 90% of the Na in the melt is higher for a Type I chondrule than for a Type II chondrule. A higher density of dust might also explain why rims appear to be more abundant and more processed around Type I chondrules.

4.3.2. Formation and accretion sequences

A specific regime of pressure and temperature is necessary for the rims to form. Indeed, isolated silicates in the matrix do not exhibit FGRs or igneous rims on their surfaces. Therefore, if chondrules and rims were formed as a result of the same transient thermal episode in high dust density environment, they accreted in a short time (∼1–100 h according to the chondrule cooling rates (Zanetta et al., 2021). In comparison, the matrix is accreted later, in a colder environment after a chondrule fragmentation episode. However, since matrix and FGRs have similar compositions, it also indicates that the time and localization of the parent body accretion were relatively restricted. Large-scale mixing is unlikely and would have modified the composition of the matrix.

5. SUMMARY AND CONCLUSIONS

In summary, we propose a general scenario for the formation of FGR and matrix in the different chondrite groups. The fine-grained dust of the nebula is thermally processed in a dense region suitable for chondrule formation. (1) The dust in the vicinity of the hot chondrules is heated to various temperatures, whose maximum may be a function of the distance to the chondrule forming region as well as of the dust density. The accretion of dust assemblages to the chondrules favors compaction and the intercalation of amorphous domains thus leading to the formation of FGRs. (2) Chondrule fragments (olivine, pyroxene, sulfides) resulting from dynamic collisions are produced in the nebula. The matrix material has escaped the thermal processing and is mixed with fragments, as well as whole chondrules with their FGR attached to form the parent bodies. (3) Aqueous alteration occurs to various extents in the parent bodies (Fig. 13). It modifies the characteristics inherited during FGR formation and progressively tends to erase the textural differences between rims and the matrix in any given chondrite. The formation of Fe-oxides, phyllosilicates and TCI occurred in the matrix of QUE 99177 (CR) and Paris (CM). The contours of the amorphous silicate domains are more difficult to distinguish in both the matrix and the FGRs of these chondrites. In DOM 08006 (CO) only Fe-rich oxides are observed as a result of aqueous alteration. In Semarkona (LL), the smooth amorphous silicate of the FGR transformed into nanocrystalline phyllosilicates which, along with the phyllosilicate in the matrix, are the most distinctive features inherited from aqueous alteration on the parent body.

Multiple stage scenarios may be considered but we would like to emphasize that the major conclusion of the present paper is that in the three chondrites studied here and in the Paris CM chondrite (Zanetta et al., 2021), FGR formation requires a thermal episode to explain the differences between their microstructure and that of the adjoining matrix. We thus showed that rims record unique information about the nebular conditions that existed at the time of chondrule formation.

Further studies would allow us to better constrain the conditions that existed at the time of FGR formation in different locations of the disk. The Fe-Mg interdiffusion in the Fe-rich olivine of DOM 08006 (CO) might be a good tracer of the conditions experienced by FGRs. In addition, we showed that FGR textures differ according to the type of the chondrule they embed. A systematic study comparing FGRs and the component they surround might also allow us to find out whether or not the thermal modification of FGRs is linked to the formation of that component.

Declaration of Competing Interest

The authors declare that they have no known competing financial interests or personal relationships that could have appeared to influence the work reported in this paper.

APPENDIX A. SUPPLEMENTARY DATA

Supplementary data to this article can be found online at https://doi.org/10.1016/j.gca.2021.11.019.

REFERENCES

Abreu N. M. and Brearley A. J. (2010) Early solar system processes recorded in the matrices of two highly pristine CR3 carbonaceous chondrites, MET 00426 and QUE 99177. *Geochim. Cosmochim. Acta* **74**, 1146–1171.

Alexander C. M. O. D., Barber D. J. and Hutchison R. (1989a) The microstructure of Semarkona and Bishunpur. *Geochim. Cosmochim. Acta* **53**, 3045–3057.

Alexander C. M. O. D., Greenwood R. C., Bowden R., Gibson J. M., Howard K. T. and Franchi I. A. (2018) A mutli-technique search for the most primitive CO chondrites. *Geochim. Cosmochim. Acta* **221**, 406–420.

Alexander, C. M. O. D., Grossman, J. N., Ebel, D. S., & rubin, F. J. (2008). The formation conditions of chondrules and chondrites. *Science*, *320*(5883), 1617-1619.

Alexander C. M. O. D., Hutchison R. and Barber D. J. (1989b) Origin of chondrule rims and interchondrule matrices in unequilibrated ordinary chondrites. *Earth Planet. Sci. Lett.* **95**, 187–207.

Berlin J., Jones R. H. and Brearley A. J. (2011) Fe-Mn systematics of type IIA chondrules in unequilibrated CO, CR, and ordinary chondrites. *Meteorit. Planet. Sci.* **46**, 513–533.

Bonal L., Quirico E., Flandinet L. and Montagnac G. (2016) Thermal history of type 3 chondrites from the Antarctic meteorite collection determined by Raman spectroscopy of their polyaromatic carbonaceous matter. *Geochim. Cosmochim. Acta* **189**, 312–337.

Brearley A. J. (1993) Matrix and fine-grained rims in the unequilibrated CO3 chondrite, ALHA77307: Origins and evidence for diverse, primitive nebular dust components. *Geochim. Cosmochim. Acta* **57**, 1521–1550.

Brearley A. J. (1999) Origin of graphitic carbon and pentlandite in matrix olivines in the Allende meteorite. *Science* **285**(5432), 1380–1382.

Brearley A. J. (2006) The Action of Water. *Meteorites and the early solar system* II, 584–624.

Brearley A. J. and Geiger T. (1991) Mineralogical and chemical studies bearing on the origin of accretionary rims in the Murchison CM2 carbonaceous chondrite. *Meteoritics* **26**, 323.

Burton A. S., Elsila J. E., Callahan M. P., Martin M. G., Glavin D. P., Johnson N. M. and Dworkin J. P. (2012) A propensity for n-ω-amino acids in thermally altered Antarctic meteorites. *Meteoritics & Planetary Science* **47**(3), 374–386.

Chizmadia L. J. and Brearley A. J. (2008) Mineralogy, aqueous alteration, and primitive textural characteristics of fine-grained rims in the Y-791198 CM2 carbonaceous chondrite: TEM observations and comparison to ALHA81002. *Geochim. Cosmochim. Acta* **72**(2), 602–625.

Ciesla F. J., Lauretta D. S., Cohen B. A. and Hood L. L. (2003) A nebular origin for chondritic fine-grained phyllosilicates. *Science* **299**(5606), 549–552.

Cliff G. and Lorimer G. W. (1975) The quantitative analysis of thin specimens. *J. Microsc.* **103**, 203–207.

Cuvillier P., Leroux H., Jacob D. and Hirel P. (2015) Fe-Mg interdiffusion profiles in rimmed forsterite grains in the Allende matrix: time-temperature constraints for the parent body metamorphism. *Meteorit. Planet. Sci.* **50**, 1529–1545.

Davidson J., Alexander C. M. O. D., Stroud R. M., Busemann H. and Nittler L. R. (2019) Mineralogy and petrology of Dominion Range 08006: A very primitive CO3 carbonaceous chondrite. *Geochim. Cosmochim. Acta* **265**, 259–278.

Desch S. J., Morris M. A., Connolly, Jr., H. C. and Boss A. P. (2012) The importance of experiments: Constraints on chondrule formation models. *Meteorit. Planet. Sci.* **47**, 1139–1156.

Dobrică E. and Brearley A. J. (2016) Microchondrules in two unequilibrated ordinary chondrites: Evidence for formation by splattering from chondrules during stochastic collisions in the solar nebula. *Meteorit. Planet. Sci.* **51**, 884–905.

Dobrică E. and Brearley A. J. (2020a) Amorphous silicates in the matrix of Semarkona: The first evidence for the localized preservation of pristine matrix materials in the most unequilibrated ordinary chondrites. *Meteorit. Planet. Sci.* **55**(3), 649–668.

Dobrică E. and Brearley A. J. (2020b) Iron-rich olivine in the unequilibrated ordinary chondrite, MET 00526: Earliest stages of formation. *Meteorit. Planet. Sci.* **55**(12), 2652–2669.

Dobrică E., Le Guillou C. and Brearley A. J. (2019) Aqueous alteration of porous microchondrules in Semarkona: Implications for hydration, oxidation and elemental exchange processes. *Geochim. Cosmochim. Acta* **244**, 292–307.

Dominik C. and Tielens A. G. G. M. (1997) The physics of dust coagulation and the structure of dust aggregates in space. *Astrophys. J.* **480**(2), 647.

Fedkin A. V. and Grossman L. (2006) The fayalite content of chondritic olivine: Obstacle to understanding the condensation of rocky material. *Meteorites early Sol. Syst.* II, 279–294.

Floss C. and Stadermann F. J. (2009) High abundances of circumstellar and interstellar C-anomalous phases in the primitive CR3 chondrites QUE 99177 and MET 00426. *Astrophys. J.* **697**, 1242.

Goodrich C. A. and Delaney J. S. (2000) Fe/Mg-Fe/Mn relations of meteorites and primary heterogeneity of primitive achondrite parent bodies. *Geochim. Cosmochim. Acta* **64**, 149–160.

Greshake A. (1997) The primitive matrix components of the unique carbonaceous chondrite Acfer 094: A TEM study. *Geochim. Cosmochim. Acta* **61**, 437–452.

Greshake A., Krot A. N., Flynn G. J. and Keil K. (2005) Fine-grained dust rims in the Tagish Lake carbonaceous chondrite: Evidence for parent body alteration. *Meteorit. Planet. Sci.* **40**, 1413–1431.

Grossman J. N. and Brearley A. J. (2005) The onset of metamorphism in ordinary and carbonaceous chondrites. *Meteorit. Planet. Sci.* **40**, 87–122.

Haenecour P., Floss C., Zega T. J., Croat T. K., Wang A., Jolliff B. L. and Carpenter P. (2018) Presolar silicates in the matrix and fine-grained rims around chondrules in primitive CO3. 0 chondrites: Evidence for pre-accretionary aqueous alteration of the rims in the solar nebula. *Geochim. Cosmochim. Acta* **221**, 379–405.

Hanna R. D. and Ketcham R. A. (2018) Evidence for accretion of fine-grained rims in a turbulent nebula for CM Murchison. *Earth Planet. Sci. Lett.* **481**, 201–211.

Hanowski N. P. and Brearley A. J. (2000) Iron-rich aureoles in the CM carbonaceous chondrites Murray, Murchison, and Allan Hills 81002: Evidence for in situ aqueous alteration. *Meteorit. Planet. Sci.* **35**, 1291–1308.

Hanowski N. P. and Brearley A. J. (2001) Aqueous alteration of chondrules in the CM carbonaceous chondrite, Allan Hills 81002: implications for parent body alteration. *Geochim. Cosmochim. Acta* **65**, 495–518.

Harju E. R., Rubin A. E., Ahn I., Choi B. G., Ziegler K. and Wasson J. T. (2014) Progressive aqueous alteration of CR carbonaceous chondrites. *Geochim. Cosmochim. Acta* **139**, 267–292.

Hellmann J. L., Hopp T., Burkhardt C. and Kleine T. (2020) Origin of volatile element depletion among carbonaceous chondrites. *Earth Planet. Sci. Lett.* **549** 116508.

Hewins R. H. (1997) Chondrules. *Annual Review of Earth and Planetary Sciences* **25**(1), 61–83.

Hewins R. H., Bourot-Denise M., Zanda B., Leroux H., Barrat J. A., Humayun M. and Marty B. (2014) The Paris meteorite, the least altered CM chondrite so far. *Geochim. Cosmochim. Acta* **124**, 190–222.

Horita Z., Sano T. and Nemoto M. (1987) Simplification of X-ray absorption correction in thin-sample quantitative microanalysis. *Ultramicroscopy* **21**, 271–276.

Housley R. M. and Cirlin E. H. (1983) On the alteration of Allende chondrules and the formation of matrix. In *In Chondrules and their Origins*, pp. 145–161.

Howard K. T., Alexander C. M. O. D., Schrader D. L. and Dyl K. A. (2014) Classification of hydrous meteorites (CR, CM and C2 ungrouped) by phyllosilicate fraction: PSD-XRD modal mineralogy and planetesimal environments. *Geochim. Cosmochim. Acta* **149**, 206–222.

Howard K. T., Benedix G. K., Bland P. A. and Cressey G. (2009) Modal mineralogy of CM2 chondrites by X-ray diffraction

(PSD-XRD). Part 1: Total phyllosilicate abundance and the degree of aqueous alteration. *Geochim. Cosmochim. Acta* **73**, 4576–4589.

Howard K. T., Benedix G. K., Bland P. A. and Cressey G. (2010) Modal mineralogy of CV3 chondrites by X-ray diffraction (PSD-XRD). *Geochim. Cosmochim. Acta* **74**, 5084–5097.

Howard K. T., Benedix G. K., Bland P. A. and Cressey G. (2011) Modal mineralogy of CM chondrites by X-ray diffraction (PSD-XRD): Part 2. Degree, nature and settings of aqueous alteration. *Geochim. Cosmochim. Acta* **75**, 2735–2751.

Hua X., Adam J., Palme H. and El Goresy A. (1988) Fayalite-rich rims, veins, and halos around and in forsteritic olivines in CAIs and chondrules in carbonaceous chondrites: Types, compositional profiles and constraints of their formation. *Geochim. Cosmochim. Acta* **52**, 1389–1408.

Hua X., Wang J. and BUSECK P. R. (2002) Fine-grained rims in the Allan Hills 81002 and Lewis Cliff 90500 CM2 meteorites: Their origin and modification. *Meteorit. Planet. Sci.* **37**, 229–244.

Huss G. R., Meshik A. P., Smith J. B. and Hohenberg C. M. (2003) Presolar diamond, silicon carbide, and graphite in carbonaceous chondrites: Implications for thermal processing in the solar nebula. *Geochim. Cosmochim. Acta* **67**, 4823–4848.

Hutchison R., Alexander C. M. O. D. and Others (1987) The Semarkona meteorite: First recorded occurrence of smectite in an ordinary chondrite, and its implications. *Geochim. Cosmochim. Acta* **51**, 1875–1882.

Imai H. and Yurimoto H. (2003) Oxygen isotopic distribution in an amoeboid olivine aggregate from the Allende CV chondrite: Primary and secondary processes. *Geochim. Cosmochim. Acta* **67**, 765–772.

Jacquet E. (2014) The quasi-universality of chondrule size as a constraint for chondrule formation models. *Icarus* **232**, 176–186.

Johansen A., Jacquet E., Cuzzi J. N., Morbidelli A. and Gounelle M. (2015) New paradigms for asteroid formation. *Asteroids IV*, 471–491.

Kadono T., Arakawa M. and Kouchi A. (2008) Size distributions of chondrules and dispersed droplets caused by liquid breakup: An application to shock wave conditions in the solar nebula. *Icarus* **197**, 621–626.

Keller L. P. (1998) A transmission electron microscope study of iron-nickel carbides in the matrix of the Semarkona unequilibrated ordinary chondrite. *Meteorit. Planet. Sci.* **33**, 913–919.

Keller L. P. and Messenger S. (2011) On the origins of GEMS grains. *Geochim. Cosmochim. Acta* **75**, 5336–5365.

Kita N. T., Nagahara H., Togashi S. and Morishita Y. (2000) A short duration of chondrule formation in the solar nebula: Evidence from 26Al in Semarkona ferromagnesian chondrules. *Geochim. Cosmochim. Acta* **64**, 3913–3922.

Kojima T. and Tomeoka K. (1996) Indicators of aqueous alteration and thermal metamorphism on the CV parent body: Microtextures of a dark inclusion from Allende. *Geochim. Cosmochim. Acta* **60**, 2651–2666.

Krot A. N. and Wasson J. T. (1995) Igneous rims on low-FeO and high-FeO chondrules in ordinary chondrites. *Geochim. Cosmochim. Acta* **59**, 4951–4966.

Krot A. N., Keil K., Scott E. R. D., Goodrich C. A. and Weisberg M. K. (2014) Classification of Meteorites and Their Genetic Relationships. *Treatise Geochemistry Second Ed.* **1**, 1–63.

Krot A. N., Libourel G., Goodrich C. A. and Petaev M. I. (2004a) Silica-rich igneous rims around magnesian chondrules in CR carbonaceous chondrites: Evidence for condensation origin from fractionated nebular gas. *Meteorit. Planet. Sci.* **39**, 1931–1955.

Krot A. N., Nagashima K., van Kooten E. M. M. and Bizzarro M. (2017) High-temperature rims around calcium–aluminum-rich inclusions from the CR, CB and CH carbonaceous chondrites. *Geochim. Cosmochim. Acta* **201**, 155–184.

Krot A. N., Petaev M. I. and Bland P. A. (2004b) Multiple formation mechanisms of ferrous olivine in CV carbonaceous chondrites during fluid-assisted metamorphism. *Antarct. Meteor. Res.* **17**, 153.

Krot A. N., Petaev M. I., Scott E. R. D., CHOI B.-G., Zolensky M. E. and Keil K. (1998) Progressive alteration in CV3 chondrites: More evidence for asteroidal alteration. *Meteorit. Planet. Sci.* **33**, 1065–1085.

Krot A. N., Zolensky M. E., Wasson J. T., Scott E. R. D., Keil K. and Ohsumi K. (1997a) Carbide-magnetite assemblages in type-3 ordinary chondrites. *Geochim. Cosmochim. Acta* **61**, 219–237.

Krot A. N., Scott E. R. D. and Zolensky M. E. (1997b) Origin of fayalitic olivine rims and lath-shaped matrix olivine in the CV3 chondrite Allende and its dark inclusions. *Meteorit. Planet. Sci.* **32**, 31–49.

Lauretta D. S., Hua X. and Buseck P. R. (2000) Mineralogy of fine-grained rims in the ALH 81002 CM chondrite. *Geochim. Cosmochim. Acta* **64**, 3263–3273.

Le Guillou C., Bernard S., Brearley A. J. and Remusat L. (2014) Evolution of organic matter in Orgueil, Murchison and Renazzo during parent body aqueous alteration: In situ investigations. *Geochim. Cosmochim. Acta* **131**, 368–392.

Le Guillou C. and Brearley A. (2014) Relationships between organics, water and early stages of aqueous alteration in the pristine CR 3.0 chondrite MET 00426. *Geochim. Cosmochim. Acta* **131**, 344–367.

Le Guillou C., Changela G. H. and Brearley A. J. (2015a) Widespread oxidized and hydrated amorphous silicates in CR chondrites matrices: Implications for alteration conditions and H2 degassing of asteroids. *Earth Planet. Sci. Lett.* **420**, 162–173.

Le Guillou C., Dohmen R., Rogalla D., Müller T., Vollmer C. and Becker H. W. (2015b) New experimental approach to study aqueous alteration of amorphous silicates at low reaction rates. *Chem. Geol.* **412**, 179–192.

Leitner J., Vollmer C., Floss C., Zipfel J. and Hoppe P. (2016) Ancient stardust in fine-grained chondrule dust rims from carbonaceous chondrites. *Earth Planet. Sci. Lett.* **434**, 117–128.

Leroux H., Cuvillier P., Zanda B. and Hewins R. H. (2015) GEMS-like material in the matrix of the Paris meteorite and the early stages of alteration of CM chondrites. *Geochim. Cosmochim. Acta* **170**, 247–265.

Lewis R. D., Lofgren G. E., Franzen H. F. and Windom K. E. (1993) The effect of Na vapor on the Na content of chondrules. *Meteoritics* **28**, 622–628.

Libourel G. and Chaussidon M. (2011) Oxygen isotopic constraints on the origin of Mg-rich olivines from chondritic meteorites. *Earth Planet. Sci. Lett.* **301**, 9–21.

Liffman K. and Toscano M. (2000) Chondrule Fine-Grained Mantle Formation by Hypervelocity Impact of Chondrules with a Dusty Gas. *Icarus* **143**, 106–125.

Liffman K. (2019) Fine-grained rim formation–High speed, kinetic dust aggregation in the early Solar System. *Geochim. Cosmochim. Acta* **264**, 118–129.

Lodders K. (2010) Solar system abundances of the elements. In *Principles and perspectives in cosmochemistry*. Springer, Berlin, Heidelberg, pp. 379–417.

MacPherson G. J., Hashimoto A. and Grossman L. (1985) Accretionary rims on inclusions in the Allende meteorite. *Geochim. Cosmochim. Acta* **49**, 2267–2279.

Marrocchi Y. and Chaussidon M. (2015) A systematic for oxygen isotopic variation in meteoritic chondrules. *Earth Planet. Sci. Lett.* **430**, 308–315.

Matsumoto Y., Wakita S., Hasegawa Y. and Oshino S. (2019) Aggregate Growth and Internal Structures of Chondrite Parent Bodies Forming from Dense Clumps. *Astrophys. J.* **887**, 248.

McCanta M. C., Treiman A. H., Dyar M. D., Alexander C. M. O. D., Rumble D. and Essene E. J. (2008) The LaPaz Icefield 04840 meteorite: Mineralogy, metamorphism, and origin of an amphibole- and biotite-bearing R chondrite. *Geochim. Cosmochim. Acta* **72**, 5757–5780.

Metzler K. (2004) Formation of accretionary dust mantles in the solar nebula: Evidence from preirradiated olivines in CM chondrites. *Meteorit. Planet. Sci.* **39**, 1307–1319.

Metzler K., Bischoff A. and Stöffler D. (1992) Accretionary dust mantles in CM chondrites: Evidence for solar nebula processes. *Geochim. Cosmochim. Acta* **56**, 2873–2897.

Metzler K., Hezel D. C. and Nellesen J. (2019) Various Size-sorting Processes for Millimeter-sized Particles in the Sun's Protoplanetary Disk? Evidence from Chondrules in Ordinary Chondrites. *Astrophys. J.* **887**, 230.

Miyamoto M., Furuta T., Fujii N., McKay D. S., Lofgren G. E. and Duke M. B. (1993) The Mn-Fe negative correlation in olivines in ALHA 77257 ureilite. *J. Geophys. Res. Planets* **98**, 5301–5307.

Morris P. L. (1980) The correction of thin foil microanalysis data for X-ray absorption effects. *Electron Microsc. Anal.* **1979**, 413–416.

Murakami T. and Ikeda Y. (1994) Petrology and mineralogy of the Yamato-86751 CV3 chondrite. *Meteoritics* **29**, 397–409.

Murata K., Chihara H., Tsuchiyama A., Koike C., Takakura T., Noguchi T. and Nakamura T. (2007) Crystallization Experiments on Amorphous Silicates with Chondritic Composition: Quantitative Formulation of the Crystallization. *Astrophys. J.* **668**, 285–293.

Nagahara H., Kushiro I. and Mysen B. O. (1994) Evaporation of olivine: Low pressure phase relations of the olivine system and its implication for the origin of chondritic components in the solar nebula. *Geochim. Cosmochim. Acta* **58**, 1951–1963.

Nakamura-Messenger K., Clemett S. J., Messenger S. and Keller L. P. (2011) Experimental aqueous alteration of cometary dust. *Meteorit. Planet. Sci.* **46**, 843–856.

Nguyen A. N., Nittler L. R., Stadermann F. J., Stroud R. M. and Alexander C. M. O. D. (2010) Coordinated analyses of presolar grains in the Allan Hills 77307 and Queen Elizabeth Range 99177 meteorites. *Astrophys. J.* **719**, 166.

Nittler L. R., Alexander C. M. O. D., Davidson J., Riebe M. E. I., Stroud R. M. and Wang J. (2018) High abundances of presolar grains and 15N-rich organic matter in CO3.0 chondrite dominion range 08006. *Geochim. Cosmochim. Acta* **226**, 107–131.

Nozawa J., Tsukamoto K., Kobatake H., Yamada J., Satoh H., Nagashima K., Miura H. and Kimura Y. (2009) AFM study on surface nanotopography of matrix olivines in Allende carbonaceous chondrite. *Icarus* **204**, 681–686.

Nuth J. A., Brearley, A. J., & Scott, E. R. (2005). Microcrystals and amorphous material in comets and primitive meteorites: Keys to understanding processes in the early solar system. In *Chondrites and the protoplanetary disk* (Vol. **341**, p. 675).

Nuth J. A. and Donn B. (1983) Laboratory studies of the condensation and properties of amorphous silicate smokes. *J. Geophys. Res. Solid Earth* **88**, A847–A852.

Nuth J. A., Hallenbeck S. L. and Rietmeijer F. J. M. (2000) Laboratory studies of silicate smokes: Analog studies of circumstellar materials. *J. Geophys. Res. Sp. Phys.* **105**, 10387–10396.

Nuth J. A., Rietmeijer F. J. M. and Hill H. G. M. (2002) Condensation processes in astrophysical environments: The composition and structure of cometary grains. *Meteorit. Planet. Sci.* **37**, 1579–1590.

Palme H. and Fegley, Jr, B. (1990) High-temperature condensation of iron-rich olivine in the solar nebula. *Earth Planet. Sci. Lett.* **101**, 180–195.

Papike J. J., Karner J. M. and Shearer C. K. (2003) Determination of planetary basalt parentage: A simple technique using the electron microprobe. *Am. Mineral.* **88**, 469–472.

Peck J. A. and Wood J. A. (1987) The origin of ferrous zoning in Allende chondrule olivines. *Geochim. Cosmochim. Acta* **51**, 1503–1510.

Pignatelli I., Marrocchi Y., Mugnaioli E., Bourdelle F. and Gounelle M. (2017) Mineralogical, crystallographic and redox features of the earliest stages of fluid alteration in CM chondrites. *Geochim. Cosmochim. Acta* **209**, 106–122.

Quirico E., Bonal L., Beck P., Alexander C. M. O. D., Yabuta H., Nakamura T., Nakato A., Flandinet L., Montagnac G., Schmitt-Kopplin P. and Herd C. D. K. (2018) Prevalence and nature of heating processes in CM and C2-ungrouped chondrites as revealed by insoluble organic matter. *Geochim. Cosmochim. Acta* **241**, 17–37.

Rietmeijer F. J. M., III J. A. N. and Karner J. M. (1999) Metastable Eutectic Condensation in a Mg-Fe-SiO-H2-O2 Vapor: Analogs to Circumstellar Dust. *Astrophys. J.* **527**, 395.

Rietmeijer F. J. M., Nuth, III, J. A. and Nelson R. N. (2004) Laboratory hydration of condensed magnesiosilica smokes with implications for hydrated silicates in IDPs and comets. *Meteorit. Planet. Sci.* **39**, 723–746.

Rubin A. E. (1984) Coarse-grained chondrule rims in type 3 chondrites. *Geochim. Cosmochim. Acta* **48**, 1779–1789.

Rubin A. E. (2010) Physical properties of chondrules in different chondrite groups: Implications for multiple melting events in dusty environments. *Geochim. Cosmochim. Acta* **74**, 4807–4828.

Rubin A. E. and Krot A. N. (1996) Multiple heating of chondrules. *Chondrules and the protoplanetary disk*, 173–180.

Rubin A. E., Scott E. R. D. and Keil K. (1997) Shock metamorphism of enstatite chondrites. *Geochim. Cosmochim. Acta* **61**, 847–858.

Rubin A. E., Trigo-Rodríguez J. M., Huber H. and Wasson J. T. (2007) Progressive aqueous alteration of CM carbonaceous chondrites. *Geochim. Cosmochim. Acta* **71**(9), 2361–2382.

Russell S. S., Connolly, Jr, H. C. and Krot A. N. (2018) *Chondrules: Records of Protoplanetary Disk Processes*. Cambridge University Press.

Schrader D. L. and Davidson J. (2017) CM and CO chondrites: A common parent body or asteroidal neighbors? Insights from chondrule silicates. *Geochim. Cosmochim. Acta* **214**, 157–171.

Scott E. R. D., Jones R. H. and Rubin A. E. (1994) Classification, metamorphic history, and pre-metamorphic composition of chondrules. *Geochim. Cosmochim. Acta* **58**, 1203–1209.

Scott E. R. D. and Krot A. N. (2014) Chondrites and Their Components. *Treatise Geochemistry Second Ed.* **1**, 65–137.

Stephens J. R. and Kothari B. K. (1978) Laboratory analogues to cosmic dust. *Moon Planets* **19**, 139–152.

Tenner T. J., Ushikubo T., Kurahashi E., Kita N. T. and Nagahara H. (2013) Oxygen isotope systematics of chondrule phenocrysts from the CO3.0 chondrite Yamato 81020: Evidence for two distinct oxygen isotope reservoirs. *Geochim. Cosmochim. Acta* **102**, 226–245.

Tenner T. J., Nakashima D., Ushikubo T., Kita N. T. and Weisberg M. K. (2015) Oxygen isotope ratios of FeO-poor chondrules in CR3 chondrites: Influence of dust enrichment and H2O during chondrule formation. *Geochim. Cosmochim. Acta* **148**, 228–250.

Varela M. E., Zinner E., Kurat G., CHU H.-T. and Hoppe P. (2012) New insights into the formation of fayalitic olivine from Allende dark inclusions. *Meteorit. Planet. Sci.* **47**, 832–852.

Vollmer C., Pelka M., Leitner J. and Janssen A. (2020) Amorphous silicates as a record of solar nebular and parent body processes—A transmission electron microscope study of fine-grained rims and matrix in three Antarctic CR chondrites. *Meteorit. Planet. Sci.* **55**(7), 1491–1508.

Wasson J. T. (1996) Chondrule formation: energetics and length scales. *Chondrules and the protoplanetary disk*, 45–54.

Weinbruch S., Palme H., Müller W. F. and El Goresy A. (1990) FeO-rich rims and veins in Allende forsterite: Evidence for high temperature condensation at oxidizing conditions. *Meteoritics* **25**, 115–125.

Weinbruch S., Zinner E. K., El Goresy A., Steele I. M. and Palme H. (1993) Oxygen isotopic composition of individual olivine grains from the Allende meteorite. *Geochim. Cosmochim. Acta* **57**, 2649–2661.

Weisberg M. K., McCoy T. J. and Krot A. N. (2006) Systematics and evaluation of meteorite classification. *Meteorites and the early solar system* **II**, 19.

Zanetta P.-M., Le Guillou C., Leroux H., Zanda B., Hewins R. H., Lewin E. and Pont S. (2019) Modal abundance, density and chemistry of micrometer-sized assemblages by advanced electron microscopy: Application to chondrites. *Chem. Geol.* **514**, 27–41.

Zanetta P.-M., Leroux H., Le Guillou C., Zanda B. and Hewins R. H. (2021) Nebular thermal processing of accretionary fine-grained rims in the Paris CM chondrite. *Geochim. Cosmochim. Acta* **295**, 135–154.

Zega T. J. and Buseck P. R. (2003) Fine-grained-rim mineralogy of the Cold Bokkeveld CM chondrite. *Geochim. Cosmochim. Acta* **67**, 1711–1721.

Zolensky M., Barrett R. and Browning L. (1993) Mineralogy and composition of matrix and chondrule rims in carbonaceous chondrites. *Geochim. Cosmochim. Acta* **57**, 3123–3148.

Zolotov M., Mironenko M. V and Shock E. L. (2006) Thermodynamic constraints on fayalite formation on parent bodies of chondrites. *Meteorit. Planet. Sci.* **41**, 1775–1796.

Associate editor: Hope Ishii